LINEAR POLARIZATION AND LIFETIME MEASUREMENTS IN ^{194}TL

Lukisi Paulus Masiteng

Thesis presented in fulfillment of the requirements for the degree of Master of Sciences at the University of the Western Cape.

Supervisor: Dr. E. A. Lawrie
Dept. of Physics
iThemba LABS

Co-supervisor: Dr. D. G. Roux
Dept. of Physics
University of the Western Cape

November 2006

DECLARATION

I, the undersigned, hereby declare that the work contained in this thesis is my own original work and that I have not previously in its entirety or in part submitted it at any university for a degree.

Signature: ....

Date: 09-03-07

Abstract

High-spin states in ^{194}Tl were populated using the ^{181}Ta(^{18}O, 5n) reaction at the beam energies of 91 and 93 MeV during two weekends of beam time. The γ-γ coincidence data associated with this reaction were measured employing the AFRODITE array, which at that time consisted of 8 clover and 6 Low Energy Photon Spectroscopy (LEPS) detectors at iThemba Laboratory for Accelerator Based Sciences (iThemba LABS).

The spectroscopy analysis of the ^{194}Tl data presented in this work involved the following analysis and measurements: gain matching, calibration, gain drift corrections and Doppler-shift corrections for one week-end of data, linear polarization and recoil shadow anisotropy (RSAM) lifetime measurements using all data. The obtained linear polarization anisotropies were used to assign parities to the levels of the existing level scheme of ^{194}Tl [Ram06]. One isomeric state at $I^{\pi} = 8^{-}$ associated with a delayed 293 keV transition was observed and its half-life was determined by using the RSAM technique to be $t_{1/2}$ = 6.9±1.0ns.

Acknowledgements

I wish to express my sincere gratitude to the following for making the realization of this thesis possible:

- First of all a warm thank to my supervisor Dr. Elena A. Lawrie for always being helpful, supportive and encouraging, and for sharing her wide knowledge and experience within the field of nuclear spectroscopy with me.
- My co-supervisor Dr. David G. Roux for his positive suggestions and discussions during the writing up of this work ;
- Dr. J. J. Lawrie, for allowing me to pursue this project in the Physics Group;
- My parents (Mr. S. S. Masiteng and Mrs. E. M. Masiteng), ke leboha ho menahane batshweneng;
- To all the postgraduates within the Physics Group especially Sifiso S. Ntshangase for a very interesting and pleasant discussions ;
- A special thank goes to all my friends, K. G. Tshabalala, M. A. Malape and B. B Mokaleng for always being supportive ;
- iThemba LABS and University of the Western Cape for the funding I received;
- Lastly, I would like to thank the God for everything.

Lukisi Paulus Masiteng. November 2006

Contents

List of Figures

List of Tables

Chapter 1

Introduction

Heavier thallium isotopes (A › 187) are situated in a region of deformed oblate nuclei and just below the spherical lead isotopes with Z = 82. A lot of in-beam γ spectroscopy work has been done on the odd-odd Tl isotopes with $192 \leq A \leq 200$ [Kre77, Kre78, Kre78, Kre80, Dup02]. These studies have shown that the yrast bands in these nuclei are associated with the $\pi h_{9/2} \otimes \nu i_{13/2}$ configuration and include low – energy transitions near their bandheads. Furthermore, experimental and theoretical studies on the heavier Hg and Tl isotopes showed that these nuclei are able to support a small and essentially oblate deformation [Mey74, New70, New74, Pro74, Tjø74, Tok75, Lie76, Lie75].

In this work the high spin states in ^{194}Tl were excited via the complete heavy-ion fusion evaporation reaction ^{181}Ta(^{18}O, 5n) ^{194}Tl at a beam energy of 91 MeV in the first weekend and 93 MeV in the second weekend. The analysis of the second weekend data lead to the considerable extension of ^{194}Tl level scheme [Ram06]. The present work made use of both the first and the second weekend of data to perform the linear polarization measurements and to search for isomeric states of ^{194}Tl using the Recoil Shadow Anisotropy method. The results of the measured linear polarization anisotropies lead to assignment of parities to most of the transitions in the previously proposed level scheme of ^{194}Tl [Ram06]. A delayed 293 keV transition was observed and its lifetime was determined by using the RSAM technique.

This thesis is organized as follows:

Chapter 2 describes the experimental equipment used,

Chapter 3 outlines the experiment and methods used for data analysis, and

Chapter 4 presents the data analysis, the results and the summary of the work presented in this thesis.

1.1 Nuclear Reaction Mechanism

1.1.1 Heavy-Ion Fusion Evaporation Reaction (HIFE)

In-beam gamma-ray spectroscopy using fusion-evaporation reactions is one of the most efficient methods for studying nuclear structure at high-spin since large angular momentum can be brought into the system. These reactions are used to excite neutron deficient nuclei up to high-spins through the use of stable beam and target combinations. In these types of reactions, the projectile fuses with the target nucleus to produce a compound system. These reactions work well when the best selection of beam energy and target – projectile combination is selected and allow very wide range of nuclei can be reached, in many cases with considerable selectivity. The properties of the nuclei are often investigated by measuring their de-excitation γ rays. For stable and not very neutron rich isotopes, information about the structure at high spin is generally deduced from α - induced reactions, Coulomb excitation (only in the case of stable isotopes), deep – inelastic or fusion – fission reactions [Wil82].

Fusion occurs at the point when the projectile carries sufficient energy to overcome the Coulomb barrier that exists between the target and the projectile nuclei. The process of HIFE is schematically shown in fig. 1.1 and it can be described as follows:

(i) Large amount of energy is brought in to accelerate the projectile nucleus to an energy that is sufficient to overcome the Coulomb barrier between it and the target nucleus.

(ii) Due to the strong interaction during the fusion process, highly excited and rapidly rotating compound nucleus is formed. This results in both the projectile and target nuclei losing their identity [Sch81].

(iii) As the compound nucleus de-excites through particle emission (neutrons, protons and α particles), it loses most of its excitation energy.

(iv) At this stage, the compound nucleus has lost sufficient energy so that its excitation energy lies below the threshold for particle emission of about 8 MeV above the yrast line [Gro67]. De-excitation of the residual nucleus continues further by γ-ray emission.

(v) the γ decay of the residual nucleus ends at its ground state.

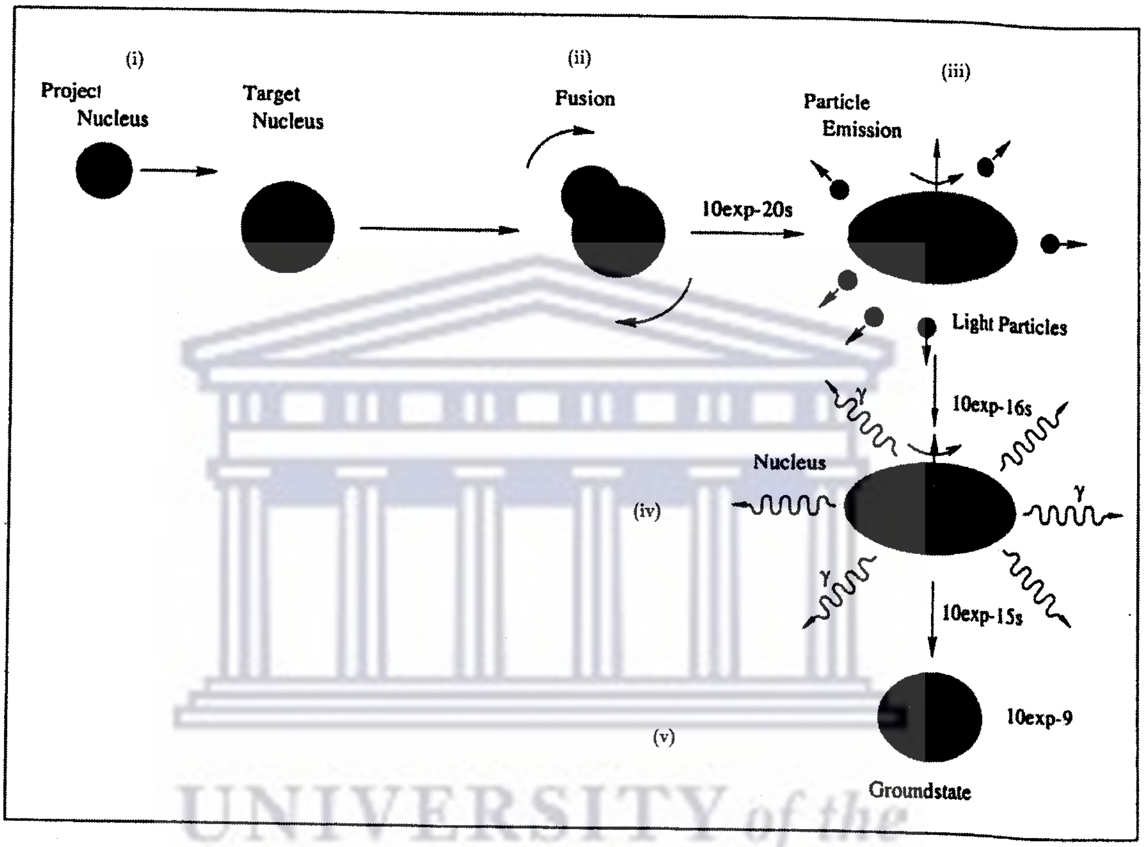

Figure 1.1: *Schematic step-by-step representation of the formation and decay of a compound nucleus through a heavy-ion fusion-evaporation reaction.*

1.1.2 Elastic Scattering and Direct Reactions

Elastic scattering can be defined as a collision in which the colliding particles only change their direction of motion, and possibly spin orientation. This means that none of the kinetic energy of the system is used to excite the colliding nuclei internally. Therefore only the direction of their motion changes while they remain in their ground state. In contrast to the fusion-evaporation reactions, the direct reactions involve direct passage from the initial to the final nuclear state without the formation of any intermediate state. The elastic and direct reactions can easily be understood when considering the fact that they occur at low and moderate bombarding energies. At low energies, the Coulomb force dominates and determines the course of a heavy-ion collision. Fig.1.2 illustrates schematically the effect of Coulomb repulsion on different trajectories near a target nucleus in a heavy-ion collision.

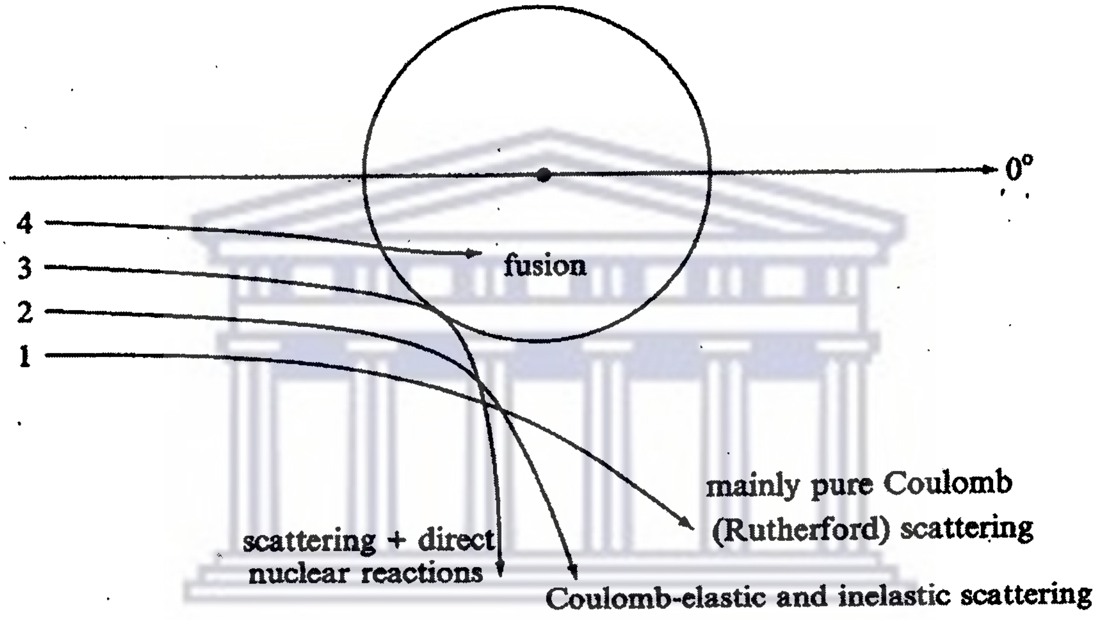

***Figure 1.2**: Effect of Coulomb repulsion on different trajectories in a heavy-ion collision. Trajectories 1 and 2 miss the nucleus and are scattered by the Coulomb field. Coulomb-inelastic excitation can also occur. On trajectory 3, the projectile grazes the nucleus during which simple, direct nuclear reactions can take place (as well as elastic and Coulomb-inelastic scattering). The projectile on trajectory 4 is shown entering the target nucleus and fusing with it. Taken from [Lil01].*

As can be seen in fig.1.2, the particles with large impact parameters, represented by trajectories 1 and 2, miss the nucleus completely and are therefore deflected away by the Coulomb field. When the system follows a grazing trajectory (path 3), the projectile just reaches the target nucleus and direct nuclear reactions begin to take place with the effect of elastic scattering being the dominant effect. There is nearly no dissipation of kinetic energy and the nuclear interaction is only a small perturbation of the Coulomb interaction. It means that only the extreme tails of the nuclear matter densities overlap during such interactions. At lower angular momenta (path 4), the projectile enters the target nucleus and more complex reactions, sometimes leading to fusion, predominate. It is therefore worthwhile to mention that this is a classical interpretation of the elastic scattering and direct reactions. It is however a well known fact that the observed behavior of heavy-ion elastic scattering is in agreement with this interpretation since its probability to occur decreases with the increase of the scattering angles. This simply means that the smaller the angle of interaction, the larger the impact parameter. Therefore the cross section $\sigma(\theta)$ follows the Rutherford formula $\sigma_{Ruth}(\theta)$ up to a certain angle because these interactions do not reach the nuclear surface. And it is beyond this point where $\sigma(\theta)$ deviates from $\sigma_{Ruth}(\theta)$ because projectiles with low impact parameter interact with the target nucleus.

1.1.3 Deep Inelastic Reactions and Limits to Fusion

In the deep inelastic scattering process, high energy projectiles scatter off the target nuclei, while transferring some energy. The nuclei may undergo also small changes in A and Z as several nucleons may be interchanged. Mainly collective states are excited by inelastic scattering. In this class of phenomena, much of the kinetic energy of the incident projectile is converted into internal energy so that the kinetic energy of the residual nuclei derives mostly from the Coulomb repulsion. Basically, in deep inelastic collisions, the two interacting nuclei are thought to be in contact for relatively long time (fig.1.3), during which the combined system rotates through an incomplete revolution before separating into two final fragments [Lil01].

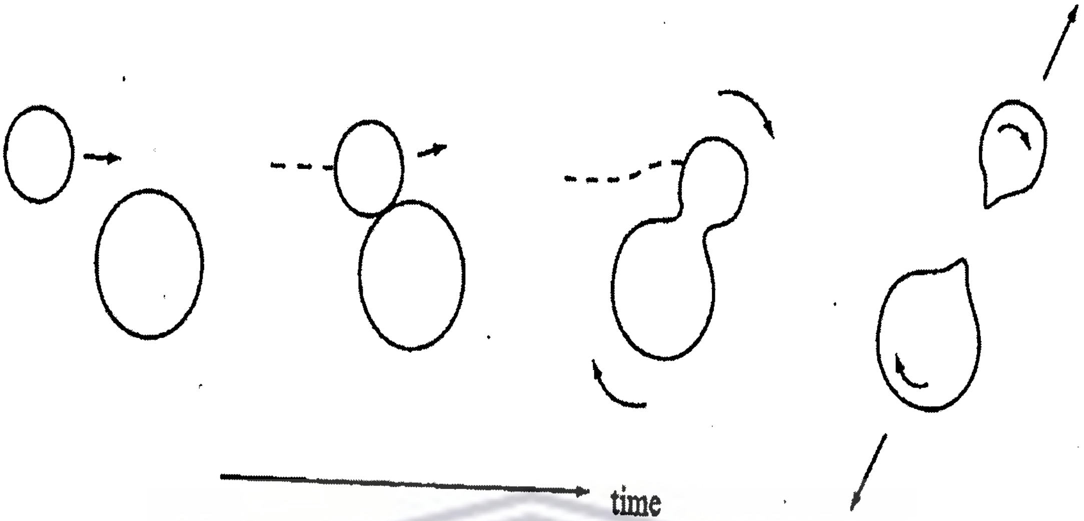

Figure 1.3: *Schematic view of a collision between two nuclei when the angular momentum is greater than can be sustained by the combined system. [Lil01].*

1.1.4 The Decay Path of an Excited Nucleus

In HIFE reactions, two heavy ions collide and combine to form a highly excited compound system with high angular momentum. A highly excited nucleus is unstable and therefore needs to get rid of its high excitation energy in one way or the other. The product may lose its excitation energy through nuclear fission. This process is mostly favoured by the heavy nuclei since the probability of its occurrence increases with mass. Lighter residual nuclei may lose its excitation energy by particle evaporation. They can either be alpha particles, protons or neutrons. However, the Coulomb barrier suppresses charged particle evaporation. As a result, mostly neutrons are evaporated. The compound nucleus is a hot many body quantum system with high angular momentum. The fact that the compound nucleus is no longer stable against centrifugal repulsion makes it de-excite very quickly ($\approx 10^{-22}$ s). In fig.1.4 the decay path of an excited nucleus is illustrated for a residual nucleus in the mass region A ~ 160. The upper thick line illustrates the high-angular momentum entry region for a heavy projectile. The residual nucleus de-excites by emitting γ-quanta, which are divided into statistical and yrast cascades (fig. 1.4).

Statistical gamma rays can be described as high energy dipole transitions, while the yrast line, (which is the minimum level energy for a given spin) is ~ 8 MeV below the particle evaporation threshold and is the region where discrete gamma rays are emitted. The emitted discrete gamma rays further carry away energy and angular momentum until the ground state is reached. It is worthwhile mentioning that discrete transitions can be isolated and studied because they are intense, and their study provides information about the properties of the nucleus [Szy83].

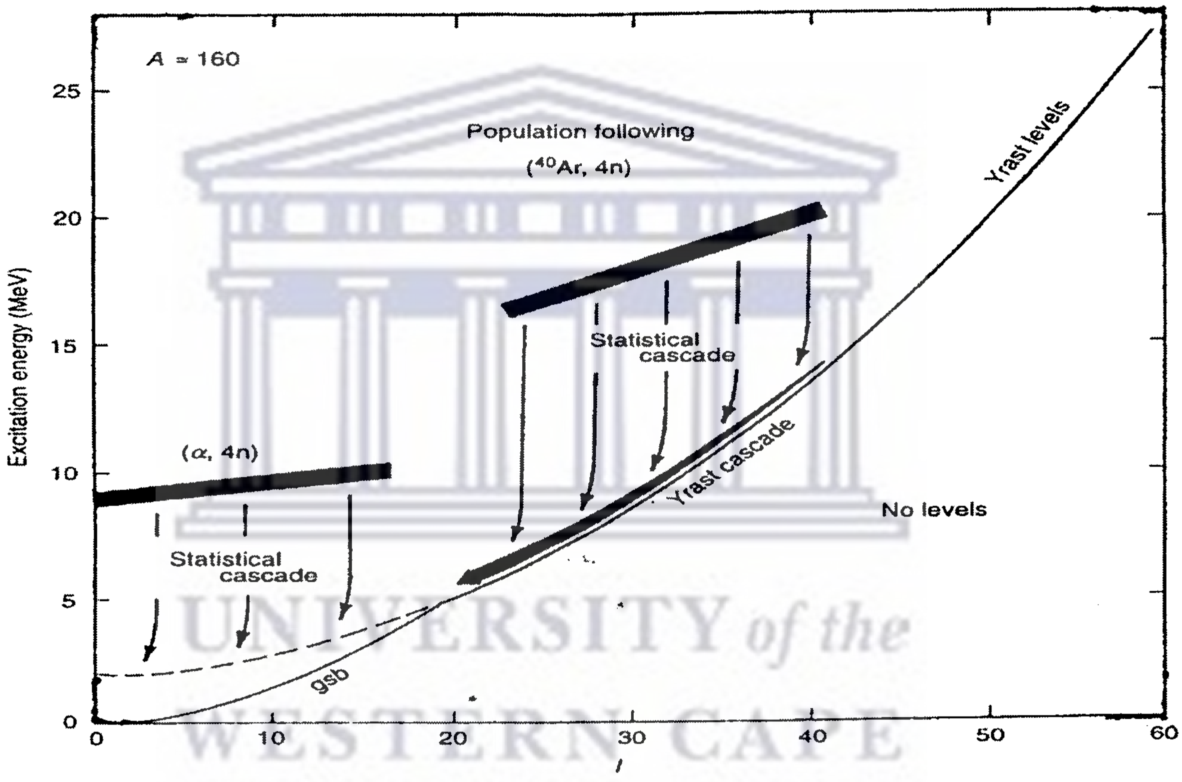

Figure 1.4: *The decay path of an excited nucleus formed in a heavy-ion fusion evaporation [Nil 95].*

1.2 Interaction of Gamma Rays with Matter

As the compound system discussed in the previous sections de-excites, it emits γ rays some of which interact with the Ge detectors placed around the target. It is therefore vital to understand the three primary interactions via which γ rays interact with matter. These three main processes are discussed in the next sections.

1.2.1 Photoelectric Absorption

Photoelectric absorption is dominant at low γ-ray energies. It arises by the interaction of the γ-ray photon with a tightly bound atomic electron. The energy of the gamma ray is transferred to the electron, which is ejected from the atom with an energy E_e given by

$$E_e = h\nu - E_b, \tag{1.1}$$

where $h\nu$ is the absorbed photon energy and E_b is the binding energy of the photoelectron in its original shell. As the photoelectron is ejected (as shown in fig.1.5), a vacancy is produced in the atomic orbital which is then filled with an electron from a higher atomic orbit. This process results in the emission of an X ray, which is itself absorbed in the material. The probability of photoelectric absorption (τ) is found to vary approximately with the atomic number (Z) of the detector material, according to:

$$\tau \propto Z^5 / E_\gamma^{3.5} \tag{1.2}$$

Therefore, high-Z materials are used for shielding against X rays and low-energy γ rays.

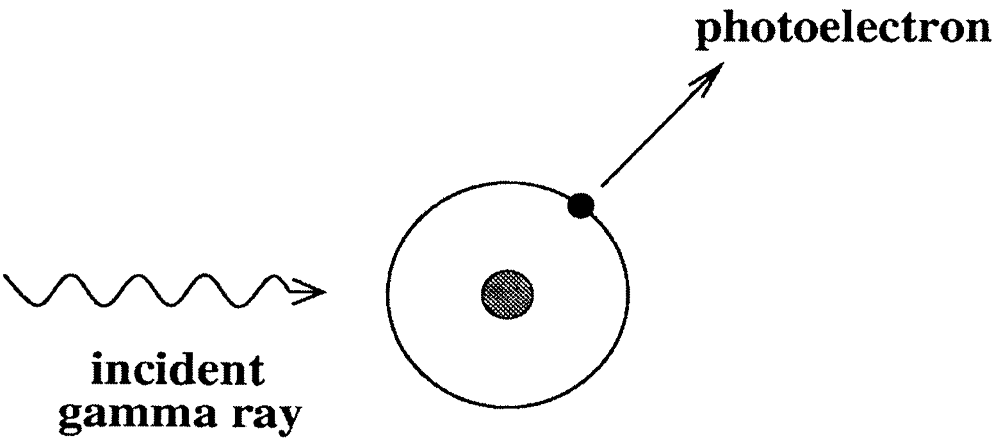

Figure 1.5: *Photoelectric absorption.*

1.2.2 Compton Scattering

Compton scattering process occurs at intermediate energies, when an incident γ ray scatters from a loosely bound electron in the absorbing material. Part of the γ-ray energy is imparted to the electron and may be described as

$$E_\gamma = E_e + E_\gamma^{'}, \tag{1.3}$$

or

$$E_\gamma^{'} = \frac{E_\gamma}{1+\left(\dfrac{E_\gamma}{m_0c^2}\right)(1-\cos\theta)}, \tag{1.4}$$

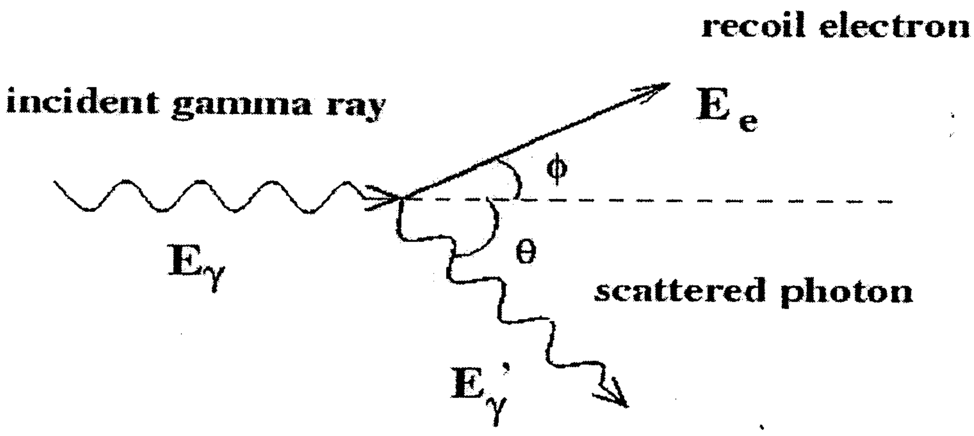

Figure 1.6: *Illustration of the Compton scattering process.*

where E_γ and E_γ' are the incident and scattered γ-ray energies, respectively, θ is the angle of the scattered photon relative to the direction of the incident photon, and m_0c^2 is the rest mass of the electron. This process is schematically illustrated in fig.1.6. From equation 1.4 it can be seen that the maximum energy is transferred to the electron when the γ ray is scattered backwards $(\theta = 180^\circ)$, but even at this value, E_e is still less than E_γ. Therefore, at all angles less than 100% of the γ-ray energy is absorbed by the detector. However, multiple scattering may occur, and this can result in a variety of energies being recorded by the detector.

1.2.3 Pair Production

In this particular process, the photon disappears and a pair of electron and positron is created. This process does not occur unless the photon has at least the energy of about 1.022 MeV. This follows from the fact that the total rest mass energy of the electron and positron is $2m_ec^2$. This process can be schematically illustrated by fig. 1.7.

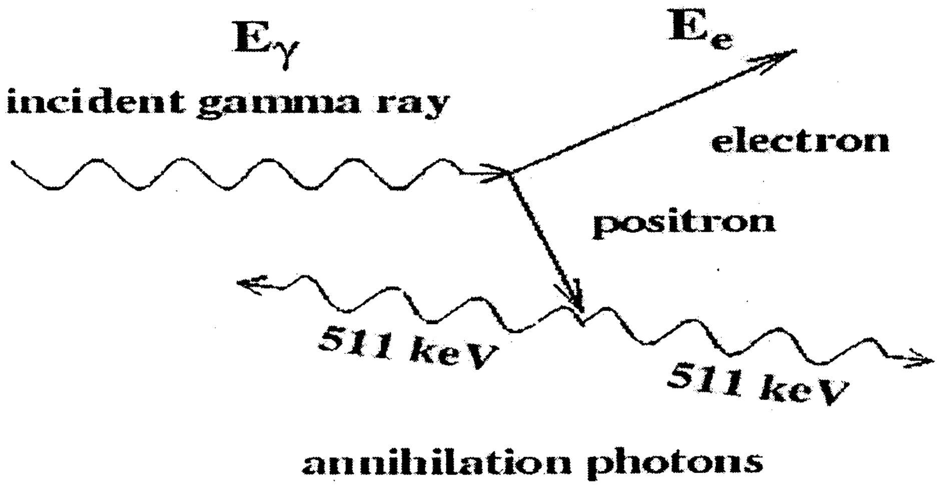

Figure 1.7: *The process of pair production.*

The most important point to note about this process is that above the threshold energy of the total rest mass of the electron and positron (1.022MeV), the probability for its occurrence increases steadily with increasing energy. Since the pair production process is the transformation of a photon into an electron positron pair, the entire photon energy is converted in the field of an atom to kinetic energy of the electron positron pair given by:

$$T_{-} + T_{+} = E - 2mc^{2}, \tag{1.5}$$

Once the electron and positron are formed, they actually lose their energy due to the collisions with atoms in the surrounding medium. This leads to the positron slowing down to very low energies and then annihilating with an electron. These two particles then disappear, and two photons with energies of 511 keV are produced. They are annihilation radiation. The pair production requires the presence of a heavy body in order for the energy and momentum to be conserved. The conservation of momentum also requires that the annihilation γ rays are emitted in opposite directions. These γ rays may in turn interact in the absorbing medium by either photoelectric absorption or Compton scattering [Lil01].

1.2.4 Attenuation Coefficients

The interaction of γ rays varies depending on the matter in which the interactions take place. This variation can be described as a function of the atomic number of the material. Fig. 1.8 shows the linear attenuation coefficients for the three processes within germanium and BGO crystals, the two γ-ray detection materials used in this work. The total linear attenuation coefficient μ_{total} is given by

$$\mu_{total} = \mu_{pe} + \mu_{cs} + \mu_{pp}, \qquad (1.6)$$

where μ_{pe}, μ_{cs}, and μ_{pp} are the attenuation coefficients for the photoelectric effect, Compton scattering, and pair production respectively. The intensity I of a γ ray absorbed within the material then becomes

$$I = I_0 e^{-\mu_{total} x}, \qquad (1.7)$$

where I_0 is the incident γ-ray energy and x is the distance traveled within the absorber. From fig 1.8 it can be seen that Compton scattering is the most predominant process for the γ-ray energies with medium energies (0.5-1 MeV).

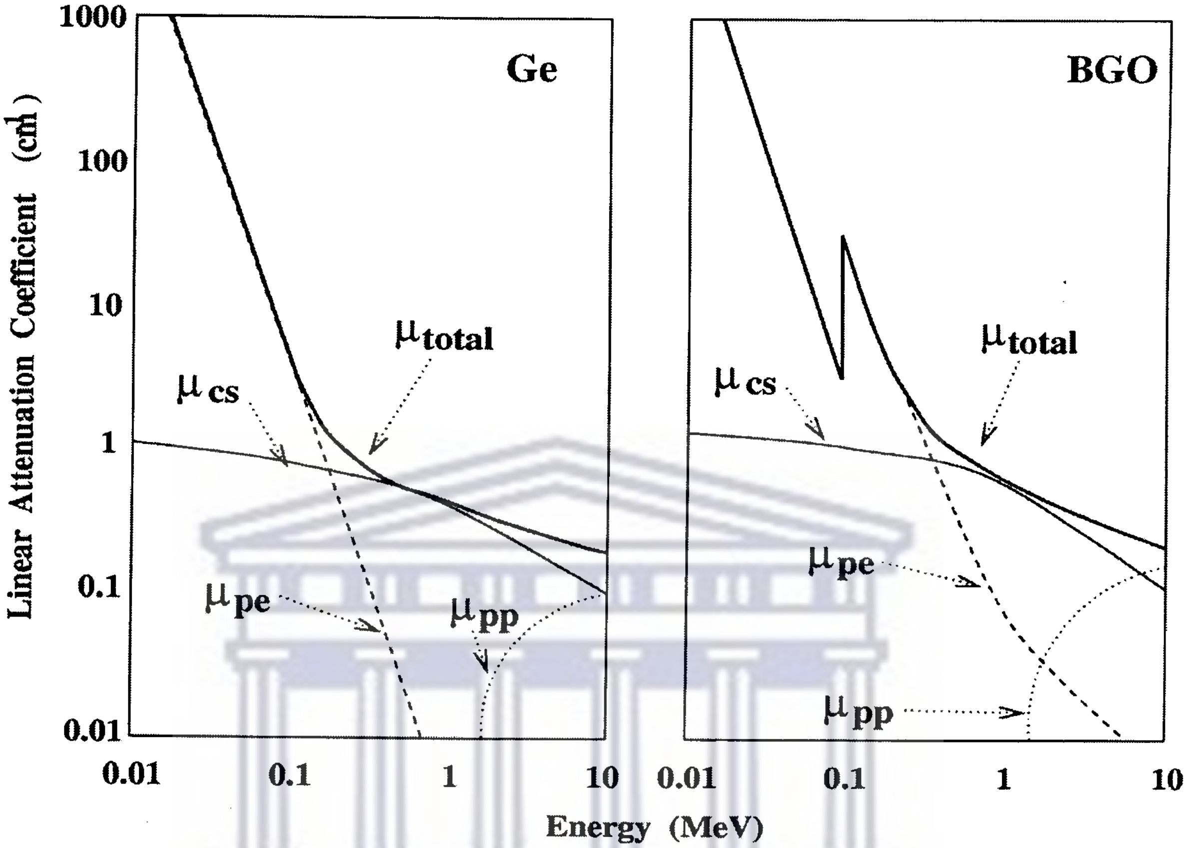

Figure 1.8: *Linear attenuation coefficients for each of the three main processes plotted against* γ*-ray energy for germanium and BGO. The total attenuation coefficient is also shown.* μ_{CS}, μ_{PE}, μ_{PP} *and* μ_{total} *are the attenuation coefficients for Compton scattering, photoelectric effect, pair production and the total, respectively.*

Chapter 2

2. Experimental Equipment

2.1 AFRODITE Array

AFRODITE is an acronym derived from AFRican Omnipurpose Detector for Innovative Techniques and Experiments [New98]. It has a capability of detecting both high and low energy photons with a reasonably high efficiency by combining two sets of high purity germanium (HPGe) detectors which are the low energy photon spectrometers (LEPS) and the clovers (shown in fig. 2.1). The AFRODITE array is supported by a rhombicuboctahedron shaped aluminium frame with 18 square and 8 triangular facets. It consists of up to 8 clover detectors (EUROGAM-Π type) and up to 8 four-way segmented LEPS detectors placed at 45°, 90° and $135^{\circ}$with respect to the beam direction. Each clover detector is surrounded by a bismuth germinate ($Bi_4Ge_3O_{12}$ or just BGO) anti Compton shield. The BGO is a highly efficient scintillator for the detection of γ-rays [Eml86, Lie84]. This arrangement provides a high total photopeak efficiency and good peak to background ratio.

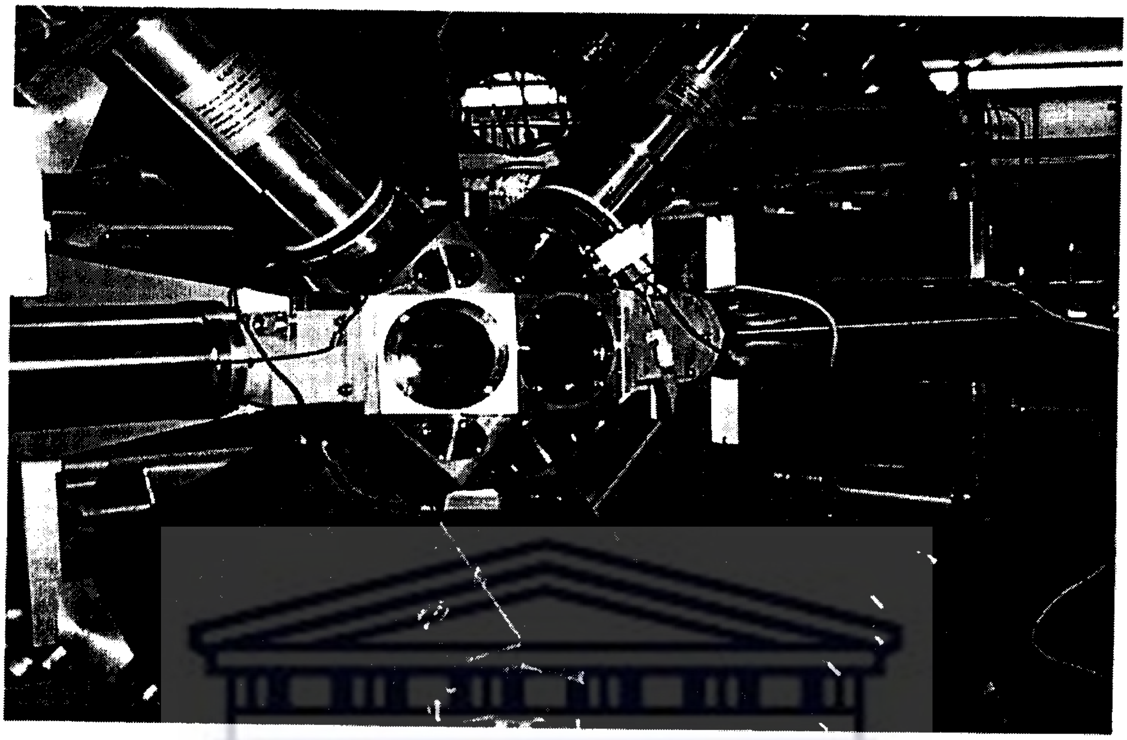

Figure 2.1: *One half of the AFRODITE array with its frame, which supports the LEPS and clover (housed inside the BGO shield) detectors. The rhombicuboctahedron-shaped target chamber has 16 kapton windows (25 micron thick and 60 mm in diameter) in total. It is supported by the beam pipe (42 mm inside diameter). The direction of the beam in the figure is from right to left.*

2.1.1 Germanium Detectors

In order for absorption of the γ rays to take place, the detector material must have a high enough absorption coefficient, which can be provided by a material of high atomic number. In addition to this, it must have a low band gap for conduction to occur, and must also have low levels of impurities in order to satisfy the conduction requirements. In our experiment germanium detectors were used because they are the best detectors for γ rays known today. The germanium detector is a semiconductor detector based on a reverse biased p-n junction [Fra86, Kno89]. As a result of the high penetration of γ rays, a large depletion region is required. In normal semiconductor detectors, this region is only ≈ 3 mm. The thickness (d) of the depletion region is given by

$$d = \sqrt{\frac{2\varepsilon V}{eN}}, \tag{2.1}$$

where ε is the dielectric constant, V the reverse bias, e the electric charge and N is the net impurity concentration. From this equation it can be seen that a decrease in the net impurity will result in an increase in the size of the depletion region. High purity germanium (HPGe) detectors have impurity levels as low as 10^9 atoms/cm^3, compared with 10^{12} atoms/cm^3 for normal semiconductors. If the remaining impurities are donor, then the crystal is $n-type$ and if they are acceptor, the crystal is $p-type.$

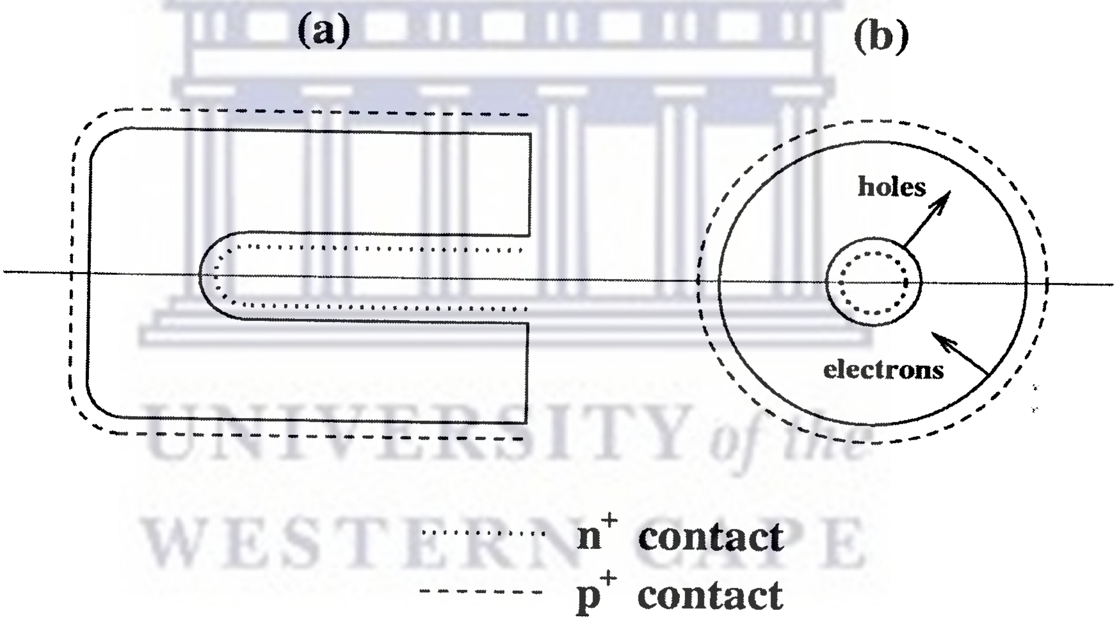

Figure 2.2: *Bulletised* $n-type$ *coaxial HPGe detector. The electrical contact surfaces are shown and (b) shows by dashed and dotted lines the motion of the electrons and the holes.*

HPGe crystal purity is not affected by temperature, allowing storage without cooling, but due to the small band gap of germanium (0.7 eV), in order to reduce thermal noise during use they must be cooled to liquid nitrogen temperature (77K). For γ-ray spectroscopy, as large an active volume as possible is required, so detectors are constructed as a bulletised coaxial shape (fig. 2.2). Part of the central core is removed and the electrical contacts are placed at the centre and on the outside of the crystal. In an $n-type$ detector, the inner contact is a thick ($\approx$ 600 μm) n^+ contact [Gil95], and the outer contact is a thin ($\approx$ 0.3 μm) p^+ contact (the $^+$ sign convention usually refers to a highly doped material [Kno89]). This is a usual arrangement for γ-ray spectroscopy since the thick n^+ contact would produce greater attenuation at the outside edge. The energy required to form an electron-hole pair in HPGe detectors is $\approx$ 3eV. This means that a large number of electron-hole pairs can be formed, and that many charge carriers are released for each γ-ray interaction. This has two consequences. Firstly there is only a small statistical fluctuation in the number of the charge carriers per pulse, and therefore a good energy resolution, and secondly, as a result of the large number of charge carriers there is an excellent signal to noise ratio. Fast neutrons can cause damage to HPGe detectors, resulting in an increase in the number of hole traps. A feature of $n-type$ detectors is that they function as electron collectors, therefore they are less susceptible to neutron damage. Neutron damaged detectors can be restored by an annealing process. In this experiment two types of Ge detectors were used, namely, clovers and LEPS detectors and they are discussed in the next sections.

2.1.2 Clover Detectors

The clover detectors currently in use in the iThemba LABS AFRODITE array comprise four n-type coaxial HPGe crystals housed in a common cryostat. A schematic view of the four HPGe crystals in a clover detector [Nol94] is shown in fig. 2.3. Clover detectors have large efficiency also for higher energy γ-rays. They have increased granularity which reduces the Doppler broadening of the peaks. Each element has its own preamplifier which allows energies deposited in more than one element of a detector due to Compton scattering to be added. This is referred to as *add-back*. By measuring the add-back in two neighbouring horizontal and vertical crystals the parities of nuclear levels can be determined (linear polarization measurements).

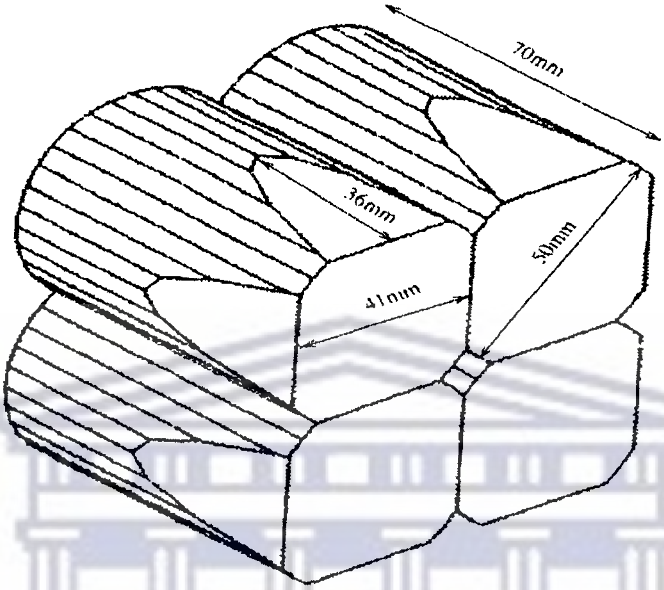

Figure 2.3: *Schematic view of the four HPGe crystals used in a Clover detector [Nol94].*

Previous studies have shown that taking into account the *add-back* enhances the clover photo peak efficiency, especially in the regime of high energy ($E_\gamma \geq 1000$keV) as shown in fig. 2.4 [New98]. The total photo-peak efficiency per clover detector is denoted by:

$$\left(E_{ph}\Omega\right)_{tot}=\sum_i\left(\varepsilon_{ph}\omega\right)_i+\sum_{i,j}\left(\varepsilon_C\omega\right)_i\left(\varepsilon_{ph}\omega\right)_j \tag{2.2}$$

where the first term on the right is the sum of the photo-peak efficiencies for each of the four crystals, and the second term is the efficiency of the clover detector in the *add-back* mode. However in the *add back* mode a decrease of energy resolution by about 0.3 keV at 1408 keV was found, compared with complete energy deposition in a single crystal element (singles modes) [Jos97]. The energy dependence of the full-width at half maximum (FWHM) for a typical single element for the clovers and LEPS of AFRODITE is shown in fig. 2.4.

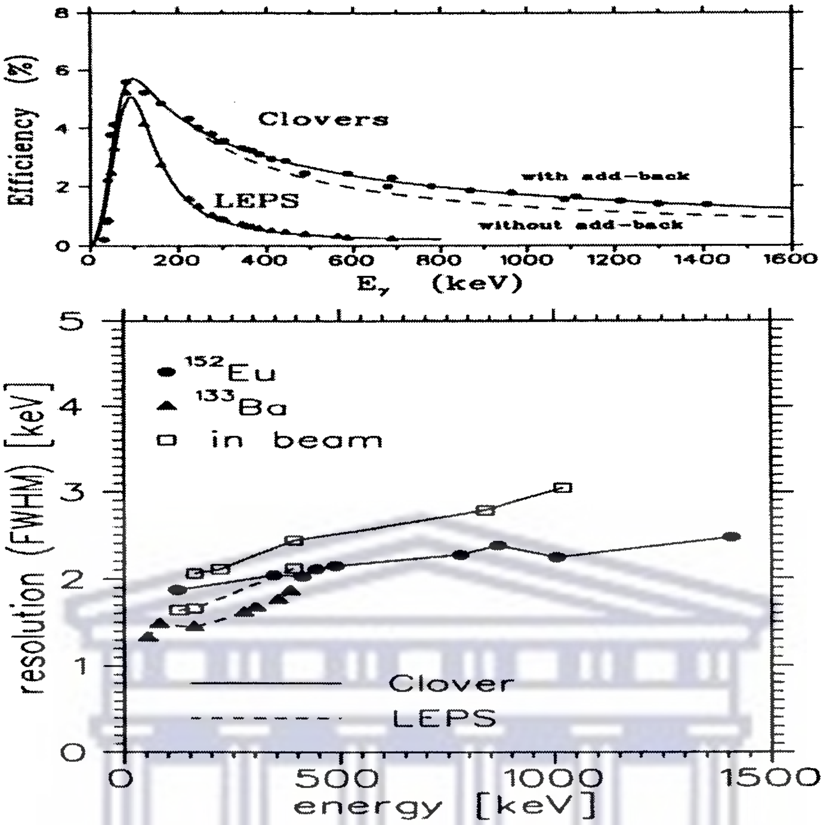

Figure 2.4: *Upper panel: Total photopeak efficiency for eight clover and 7 LEPS detectors. Lower panel: Typical single-element energy resolution for clover and LEPS detectors in the AFRODITE array. From [New98].*

2.1.3 The LEPS

The LEPS (Lower Energy Photon Spectrometer) have a planar configuration and are made from a single crystal of p-type HPGe having 10 mm thickness and 60 mm diameter with electrically segmented four quadrants. The signal from each quadrant is independently processed, as in the case of clovers. The LEPS, due to their planar shape, are most effective at lower energy (see fig. 2.4). The LEPS are mostly used to determine X-rays and low-energy γ rays. Low energy photons are less likely to undergo Compton scattering and as a result of this LEPS are neither BGO-suppressed nor operated with add-back mode. Table 2.1 gives some detailed specifications of the AFRODITE.

Table 2.1: *Important technical specifications of the AFRODITE detectors [New98].* S_{tc} is the distance from the target center to the crystal surface.

	Clover	BGO Shield	LEPS
Number at iThemba LABS	8	8	8
type	HPGe	BGO	HPGe
Entrance window			300μm Be
length	71 mm	~26 cm	10 mm
diameter	51 mm		60 mm
S_{tc}	196 mm		119 mm
Solid angle per detector (in % of 4π)	1.57 %		1.34 %

2.1.4 Escape Suppressed Spectrometer

Compton suppression can vastly improve the peak to total ratio in a γ-ray spectrum. Thus very often HPGe detectors are surrounded by a scintillator shield, and this combination is termed an escape suppressed spectrometer (ESS). A schematic of an escape suppressed spectrometer can be seen in fig. 2.5. The principle of the escape suppressed spectrometer is that when a γ ray is scattered outside the HPGe crystal, the shield will detect this γ ray and veto it as a bad event. This decreases the background in the spectrum and thus improves the peak to total ratio.

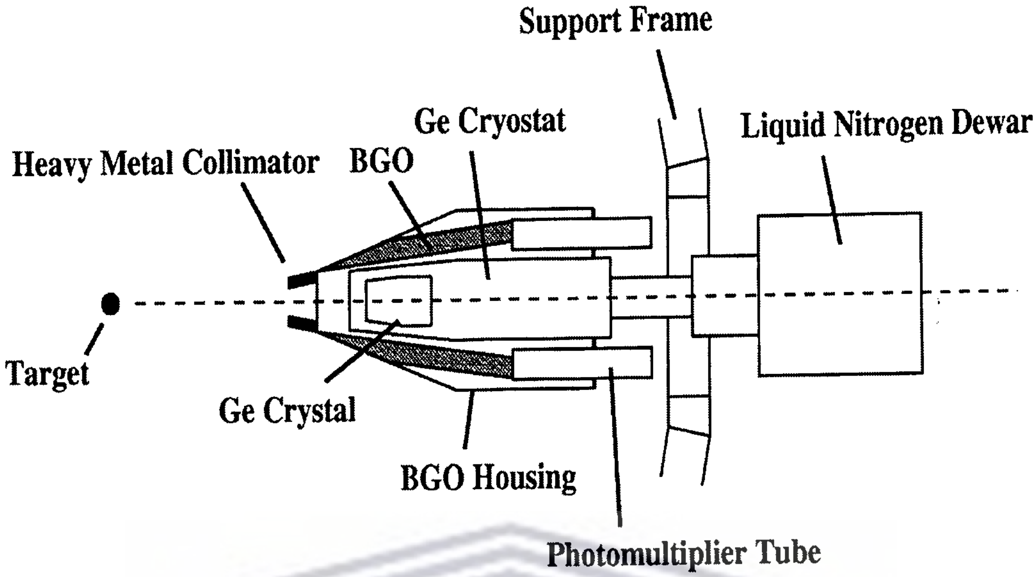

Figure 2.5: *A schematic of an escape suppressed spectrometer as used in modern γ-ray detector array.*

2.1.5 Bismuth Germanate (BGO) shield

A bismuth germinate (BGO) is placed around each clover detector of AFRODITE to reduce the outside scattering of photons which form the Compton background in the spectrum. The BGO is a pure inorganic scintillator. The large atomic number of Bi (Z=83) and high density (7.3 g/cm^3) makes it ideal for the detection of γ rays. The BGO is used when the need for high γ-ray counting efficiency outweighs the need for energy resolution. Each BGO Compton suppression shield consists of 8 optically separated segments, each having 2 PM tubes which are connected together in parallel. The BGO signal from a Compton-scattered event vetoes the associated clover. Fig. 2.6 shows the Compton background with and without the BGO shield.

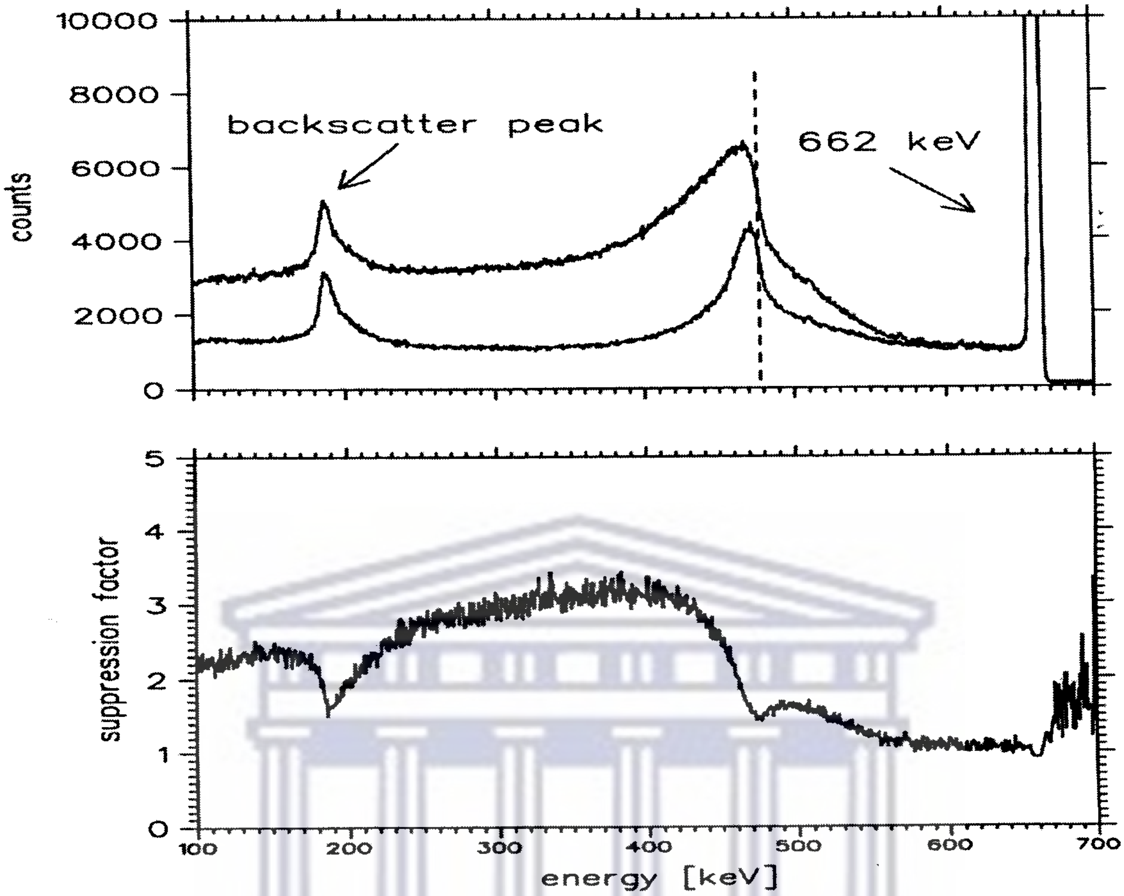

Figure 2.6: *Top panel: suppressed and unsuppressed spectra measured by placing a ^{137}Cs source at the target position of AFRODITE. The dashed line shows the location of the Compton edge. Bottom panel: suppression factors calculated from the data shown in the top panel [New98].*

As can be seen, the Compton background in the unsuppressed spectrum is larger than this in the suppressed one. It is important to note that the energy resolution of a BGO detector is quite low and as a result it cannot be used alone in high-precision energy measurements.

2.1.6 The Electronics and Data Acquisition System

Standard Nuclear Instrumentation Module (NIM) and Computer Automated Measurements and Control (CAMAC) units were used to set up the circuit depicted in fig. 2.7. The NIM and CAMAC modules perform signal processing. The MIDAS software package is employed for various task before (adjusting the ADC thresholds for clovers and BGOs) and during the experiment (data acquisition, monitoring on-line spectra and event rates). The electronic circuit diagram illustrated in fig. 2.7 consists of two sub-circuits, namely, energy and a timing circuit. The details of the entire circuit with relevant hardware as given in Table 2.1 can be found else where [Ram06].

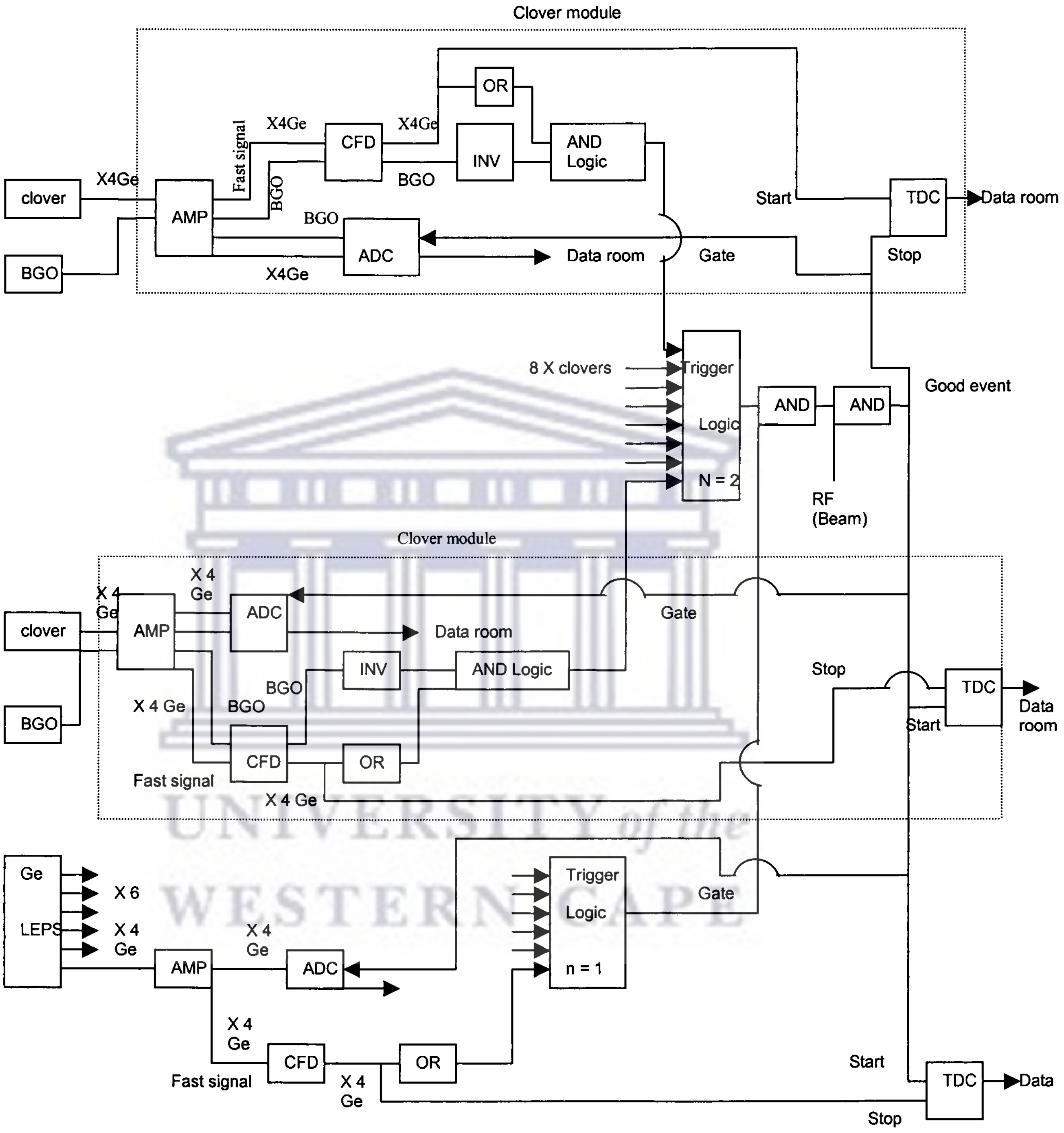

Figure 2.7: *Schematic of the AFRODITE array electronics*

Table 2.2: *Electronic modules used for the AFRODITE array*

Module	Model
Analogue-to-Digital Converter (ADC)	Silena 4418/V
Clover Module	RIS
Coincidence Unit	iThemba LABS
Discriminator	Phillips 711 or LeCroy 821
Dual Gate Generator (DGG)	LeCroy 222
Event Trigger	iThemba LABS
Logic Fan-In/Fan-Out (FIFO)	LeCroy 429
NIM-ECL converter	EDA54 (iThemba LABS)
Quad Four-Fold Logic Unit (QFFLU)	Phillips 755
Spectroscopy Amplifier	CAEN N568
Stretcher	iThemba LABS
Time Amplifier Converter (TAC)	Silena 4418/T
Timing Filter Amplifier (TFA)	Ortec 474

Chapter 3

3. Experiment and Data Analysis

3.1 Experiment

The experiment was performed at iThemba Laboratory for Accelerator Based Sciences. A stable ^{18}O beam with energy of 93, 91 MeV at the current of 20-60 nA was delivered by the Separated Sector Cyclotron facility. The target was a stack of three and two metallic tantalum foils (99.988% ^{181}Ta), used in the first and second weekend respectively, with thickness of 0.5 mg/cm^2 each. Two foils were used in the second weekend because the third one got broken after the first weekend. A thin target was used in order to avoid Doppler broadening of the peaks. Gamma rays emitted from the high-spin states of the produced nuclei were detected by the AFRODITE array. In this experiment the AFRODITE array composed of 8 clover detectors and 6 LEPS. These detectors were placed around the target in rings at 45°, 90° and 135° relative to the beam direction. In order to obtain the excitation function of the ^{181}Ta(^{18}O ,5n)^{194}Tl fusion evaporation reaction, predictions were made using the PACE4 statistical model calculations [Gav80, Gav93]. The 5n exit channel was found to peak at about 91 MeV. Fig. 3.1 shows the excitation function for this reaction. This experiment ran for two week-ends. The trigger logic was set to accept events when at least two clover detectors fired in coincidence.

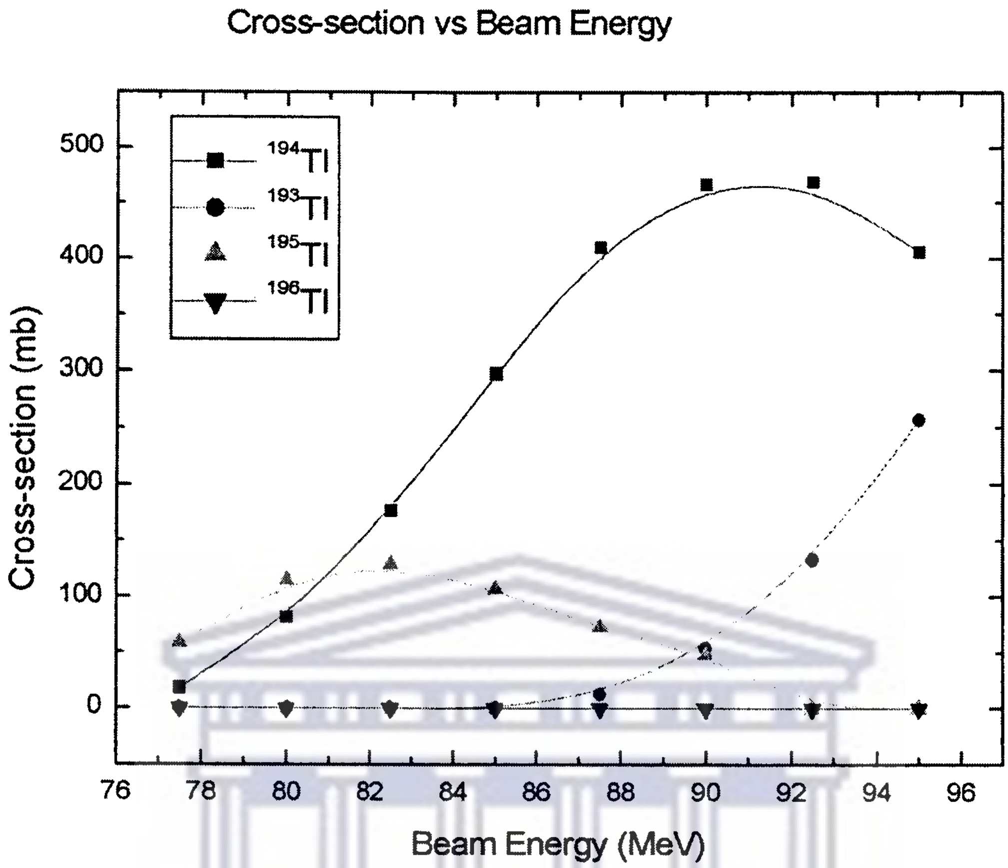

Figure 3.1: *The excitation function predicted by the statistical – model code PACE4 [Gav80, Gav93].*

The counting rate of about 7 KHz was achieved. A summary of the experimental details is presented in Table 3.1.

The data acquisition used for this experiment was based on MIDAS software package. The on – line spectra and event rates were monitored during the experiment. Both the timing and energy data were written on the digital linear tapes (DLT). With the intervals of two hours, the on – line spectra were saved on the hard disc.

Table 3.1: *Summary of the experimental details*

90° detectors	4 Clovers, 3LEPS
45° detectors	3 LEPS
135° detectors	4 Clovers
Target	^{181}Ta
Beam	^{18}O
Beam-burst separation	69ns
Beam energy	93MeV, 91 MeV
Pulse selection	No
Beam intensity	20-60nA
Recoil velocity v/c %	0.80
Compound system	^{199}Tl
Dominant residuals at 93 MeV (PACE4)	^{194}Tl(79.9%), ^{195}Tl(6.45%), ^{193}Tl(9.21%), ^{194}Hg(2.62%), ^{195}Hg(0.54%), ^{192}Au(0.44%), ^{191}Au(0.84%)
Cross section in mb (PACE4)	520 mb
Grazing angular momentum (PACE4)	36 $\hbar$
Event Trigger Condition	N≥ 2
Count Rate	7 KHz
Readout	CAMAC
Beam Time	2 weekends

3.2 Data analysis

3.2.1 Gain matching and Energy calibrations of the detectors

When using an array of germanium detectors it is important to have the possibility of summing the data from all detectors. Thus gain adjustment and absolute energy calibration are needed for all individual detectors in order to be able to deduce the energies of the newly observed γ-ray transitions. For this reason, data with standard radioactive sources of ^{152}Eu and ^{133}Ba were collected. Gain matching coefficients were obtained by fitting the source spectra and used to produce aligned one dimensional spectra for each detector. Linear gain matching was employed, thus, the two gain matching coefficients correspond to an off-set and a gain for each detector.

3.2.2 Gain-drift corrections

As part of the data analysis gain drifts that might have occurred during the entire period of the experiment were investigated and corrected. This is the variation of the peak position with respect to its initial position during the experimental run time. (i.e. the centroids of the peaks might be changing from run to run). In the first weekend experimental data gain drifts of up to ± 1 keV were observed between some of the runs while in the second weekend drifts of up to ± 2 keV were found [Ram06]. As a base for one to perform this kind of analysis, a reference spectrum which is usually obtained from the first run for the LEPS and clover detectors, is needed. A reference spectrum needs to be a gain matched and calibrated spectrum. The gain drifts in clovers and LEPS are usually found to be a linear function of the channel number. To correct the observed gain drifts new calibration coefficients represented by a' and b' in equation 3.1 and 3.2 were calculated. In these equations the centroids of the two reference peaks P_1 and P_2 are related with their corresponding shifts in a following run denoted by S_1 and S_2. In this relation the initial calibration coefficients are denoted by a and b.

$$a' = a\frac{P_2 - P_1}{P_2 + S_2 - P_1 - S_1} \tag{3.1}$$

$$b' = \frac{1}{2}\frac{P_1 S_2 - P_2 S_1}{P_2 + S_2 - P_1 - S_1} + b\frac{P_2 - P_1}{P_2 + S_2 - P_1 - S_1} \tag{3.2}$$

The final parameter a' is the slope (or gain) and b' is the offset. The new coefficients were then used to resort the data. The previously gain drifted peaks were then observed at the same channel numbers with the reference spectrum. Only two reference peaks are needed because linear gain drifts are observed.

3.2.3 Doppler-Shift Corrections

The performance of γ-ray spectrometers is often limited by the Doppler broadening of the lines due to the fact that photons are emitted while the recoiling nucleus is in flight. The use of a thin target has the consequence that γ rays emitted by the recoiling nuclei will be subjected to energy shift. The well known expression for the Doppler shift gives the observed energy E_γ:

$$E_\gamma = E_\gamma^0 \frac{\sqrt{1-\beta}}{1-\beta\cos\theta} \approx E_\gamma^0(1+\beta\cos\theta), \qquad (3.3)$$

where E_γ^0 is the unshifted energy of the emitted γ-ray, β is the recoil speed expressed as a fraction of the speed of light, and θ is the angle between the recoil velocity and the direction of the observation of the γ ray. Therefore, in order to obtain the correct γ-ray energy, Doppler shift corrections were performed. From the above equation, it can be seen that maximum Doppler shift will be observed for θ = 0° and 180°. Assuming that the detector covers an infinitesimal solid angle the energies of all monoenergetic photons observed in the same detector would be shifted by the same amount with respect to the energies of the emitted photons. Since real detectors cover a finite solid angle, photons will interact within a finite angular range $[\theta-\Delta\theta, \theta+\Delta\theta]$ and the effect will be that the photopeak will shift and also broaden. In our experiment the recoil velocity was measured as $\beta \approx 0.80 \pm 0.04\%$ [Ram06].

3.2.4 Construction of a γ-γ coincidence matrix

The gain matching coefficients obtained after the gaindrift and Doppler shift corrections corrected for any misalignment in the experimental data. At this point, the data were ready to be sorted into $E_\gamma - E_\gamma$ matrix. The $\gamma-\gamma$ coincidences which occur when two or more γ rays (e.g. $E_{\gamma1}$ and $E_{\gamma2}$) are detected during a resolving time (coincidence window) of about 150 ns in our experiment, are used to construct a 2-deminsional symmetric matrix with E_γ on the x and y- axes and coincidence counts on the z-axis. The standard procedure in constructing a matrix is to use the detected coincidence events. An event constitutes all γ-rays detected in coincidence (i.e. within the resolving time). To get a clear picture of the $E_\gamma - E_\gamma$ matrix, let us consider a coincidence event of three γ-rays, say $E_{\gamma 1}$, $E_{\gamma 2}$ and $E_{\gamma 3}$. From this coincidence event, we then can form all possible coincidence pairs e.g. ($E_{\gamma 1}$, $E_{\gamma 2}$) and ($E_{\gamma 2}$, $E_{\gamma 1}$), ($E_{\gamma 1}$, $E_{\gamma 3}$) and ($E_{\gamma 3}$, $E_{\gamma 1}$), ($E_{\gamma 2}$, $E_{\gamma 3}$) and ($E_{\gamma 3}$, $E_{\gamma 2}$). The coincidence pairs are represented in a matrix by coordinates (x , y , z). This basically means that the pair ($E_{\gamma 1}$, $E_{\gamma 2}$) corresponds to coordinates ($E_{\gamma 1}$, $E_{\gamma 2}$, z_1), and the pair ($E_{\gamma 2}$, $E_{\gamma 1}$) corresponds to coordinates ($E_{\gamma 2}$, $E_{\gamma 1}$, z_2). The number of instances the pair ($E_{\gamma 1}$, $E_{\gamma 2}$) is found in the data is denoted by z_1, which represents counts on the z-axis. Similarly z_2 represents the number of instances the pair ($E_{\gamma 2}$, $E_{\gamma 1}$) is detected in the data. This argument implies that $z_1 = z_2$, and therefore the matrix is symmetric. During the data sorting for every instance a coincidence pair e.g. ($E_{\gamma 1}$, $E_{\gamma 2}$) is detected in the data, the coincidence counts coordinate z_1 is incremented.

In addition, asymmetric matrices for the polarization, RSAM and DCO measurements were generated. As an example, let us consider the asymmetric DCO matrix. If we have a coincidence events of two γ-rays, say $E_{\gamma 1}$ detected at 90° and $E_{\gamma 2}$ detected at 135° and if the γ-rays detected at 90° are placed on the x-axis and those detected at 135° on the y-axis, the number of counts in the matrix will be incremented for each pair at (x, y)= ($E_{\gamma 1,}$ $E_{\gamma 2}$).

All the constructed matrices are gated on time. This ensures that only the coincidence events of γ rays from residual nuclei produced by a particular beam pulse detected in the same reaction are studied.

3.2.5 Gating

The slicing of a region around a γ-ray energy E_γ on the x-axis or y-axis in a $E_\gamma - E_\gamma$ matrix is referred to as gating. This simply projects all the γ rays in coincidence with the

γ-ray with energy E_γ into a one-dimensional spectrum. By inspection of different gates on different γ-ray energies, the level scheme of a particular nucleus can be determined.

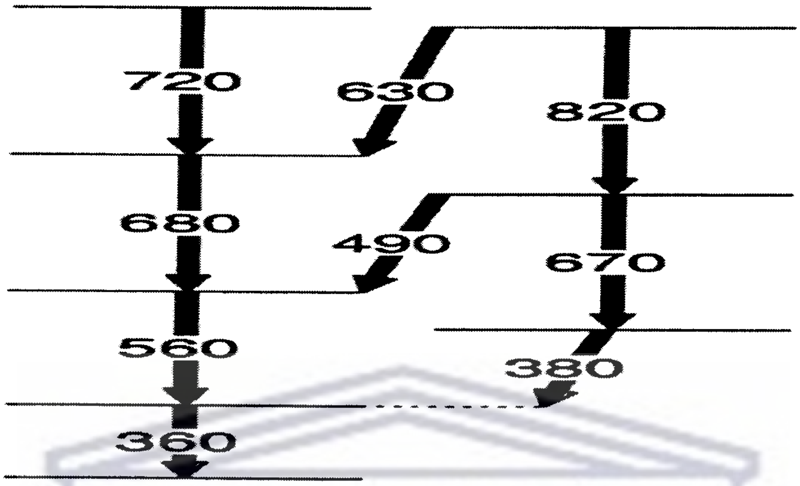

Figure 3.2: *Part of a level scheme.*

Fig. 3.2 shows a typical example of a level scheme. In this level scheme, if a gate is set on the 360 keV transition, then all the γ-rays in this level scheme can be seen in this gated spectrum, because they are in coincidence with the 360 keV transition. However, if the gate is put on the 560 keV transition, the 670 keV and the 380 keV γ-rays cannot be seen in the gated spectrum because they are not in coincidence with it. However, if a nuclear level is isomeric (with lifetime longer than the coincidence window) it is possible that the transitions that de-excite this level may end up outside the coincidence window. The solution to such a case is to tie together the γ rays below and above the isomeric state by increasing the width of the coincidence window.

3.2.6 Construction of the Level Scheme

By setting γ-energy gates on one axis of the $E_\gamma - E_\gamma$ matrix and observing the γ-lines in coincidence, the level scheme of a nucleus can be built. Basically, the construction of the level scheme involves studying the $\gamma - \gamma$ coincidence relationships between the detected γ-rays from the background subtracted coincidences spectra. This analysis is done with the aid of the ESCL8R [Rad95] software program. Using this procedure, the level scheme of ^{194}Tl isotope was built [Ram06]. The total projection spectrum of the clover matrix obtained in this experiment is shown in fig. 3.3

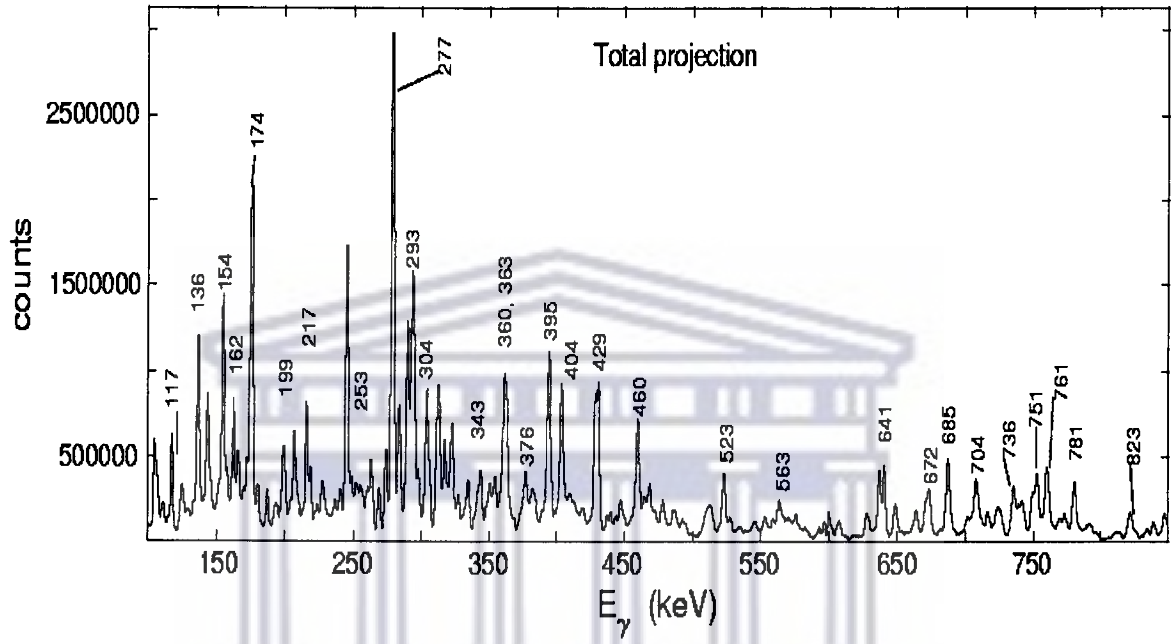

Figure 3.3: *The total projection spectrum obtained from the clover* $\gamma - \gamma$ *matrix.*

3.2.7 DCO Ratios

To determine the multipolarities of the observed transitions Directional Correlation from Oriented nuclear states (DCO) [Kra73, Dri90] $\gamma - \gamma$ matrices were constructed from the clover data. Using the fact that the AFRODITE clover detectors are positioned at 90° and 135° with respect to the beam direction, two types of $\gamma - \gamma$ coincidence matrices were constructed: (i) An asymmetric matrix which consisted of the coincidences between γ-rays detected at 135° (y-axis) and those detected at 90° (x-axis), and (ii) A symmetric which matrix consisted of coincidences between γ rays at 135° only. The same gate was set on the y-axis (135°) in both matrices to produce gated spectra. Gates were set on the photopeaks and on the background region close by, such that background – subtracted spectra, S(135°) and S(90°) could be made. The DCO ratios for the γ-rays of interest were determined as:

$$R_{DCO} = \frac{A(135^\circ)}{A(90^\circ)} \qquad (3.4)$$

where $A(135^\circ)$ is the area of the peak of interest in the S(135°) and $A(90^\circ)$ is the area of the peak in the S(90°) spectra. By taking the ratio of the number of counts for a given transition in these two spectra, a DCO ratio can be obtained, which can be used to distinguish between different multipole orders. The R_{DCO} for a number of known dipole and quadrupole transitions in ^{194}Tl [Kre79] were calculated from these background subtracted spectra. Average R_{DCO} values of 0.5 and 0.8 were obtained for the known stretched dipole ($\Delta I = 1$) and stretched quadrupole ($\Delta I = 2$) transitions respectively. The obtained values of the R_{DCO} were used to assign the spins to newly observed transitions. These measurements were done in the analysis of the second weekend data [Ram06].

3.2.8 Linear Polarization Measurements

In order to assign parities to the transitions in the level scheme of ^{194}Tl [Ram06] and to determine if the observed γ rays are either electric or magnetic, linear polarization measurements were conducted. This kind of analysis was made possible by the presence of the clover detectors at right angles to the beam direction [Fag59, Lit70, But73, Sim83, Sch94, Sch98]. The measured experimental anisotropy, A_p of the γ-rays is related to the degree of linear polarization, P by:

$$P = \frac{1}{Q(E_\gamma)} A_p , \qquad (3.5)$$

where Q (E_γ) is the quality factor of the polarimeter which corresponds to the polarization sensitivity of the detector. The electric or magnetic nature of the transitions is deduced from the sign of the anisotropy, A_p given by:

$$A_p = \frac{N_V - \alpha N_H}{N_V + \alpha N_H}, \tag{3.6}$$

where N_V is the number of γ-rays scattered in a plane perpendicular to the beam direction, N_H the number scattered in a plane parallel to the beam direction and α is the relative efficiency (= 1.0 in this measurement). Based on the determined linear polarization anisotropies and R_{DCO}, γ-ray transitions were assigned the multipolarity, mostly either M1 or E2.

To be able to measure γ-ray polarization it is better to examine gated spectra, which comprise only transitions from the nucleus under study. In order to do this 1-dimensional γ-ray spectra were generated from the polarization matrices. The "vertical" ("horizontal") matrix was constructed from coincidences between vertically (horizontally) scattered γ rays in the clover detectors at 90° (placed on the x-axis) and any other γ rays (placed on y-axis). Gates were set on "clean" peaks on the y-axes of both matrices. Background spectra were created by setting a gate on a background region close to the peak and then subtracted from the gated spectra to create background-subtracted spectra. These gated background-subtracted spectra of vertically and horizontally scattered events were used to measure the polarization anisotropy.

3.2.9 RSAM Lifetime Measurements

In order to search for isomeric states with lifetimes in the range of a few nanoseconds in the ^{194}Tl isotope, the Recoil Shadow Anisotropy Method (RSAM) [Gue01] was used. It was possible to carry out this kind of measurement following the fact that our experiment was performed with a thin target and the clovers of the AFRODITE array were collimated. In principle, the collimators impose a shadow effect on the clovers of the array for the delayed γ rays emitted from the recoiling residual nuclei (see fig. 3.4). The fact that the prompt transitions are detected through the same solid angles by the un-shaded and shaded clover elements, while for the delayed transitions a difference in the counting rate appears due to the collimator shadow, makes it easy to identify nanosecond isomers by simply generating the difference between the spectra of the shaded and the un-shaded elements. In the case of AFRODITE, the clover elements located at 84° with respect to the beam direction are shaded and those at 96° are un-shaded. This means that only delayed transitions will be observed in the difference spectrum. The anisotropy (A_{RSAM}) for the γ-ray transitions can be determined by using the formula:

$$A_{RSAM} = \frac{N_U - \alpha N_S}{N_U + \alpha N_S}, \tag{3.6}$$

where N_U is the number of the γ-rays detected in the un-shaded clover elements, N_S the number detected in the shaded elements and α is the relative efficiency.

Furthermore, RSAM matrices were generated for both the un-shaded and shaded elements placed at 96° and 84° respectively. The un-shaded matrix consists of coincidence events between γ-rays detected at 96° (placed on the x-axis of the matrix) and γ-rays detected at any angle (placed on the y-axis of the matrix). The shaded matrix is composed of coincidence events between γ-rays detected at 84° (placed on the x-axis of the matrix) and those detected at any angle (placed on the y-axis of the matrix). By gating on the y-axes of both matrices gated spectra were created. Background spectra created by gating on a background region close to the peak, were then subtracted from these gated spectra to create gated background-subtracted spectra, which were used to calculate the RSAM anisotropy and to search for isomeric states.

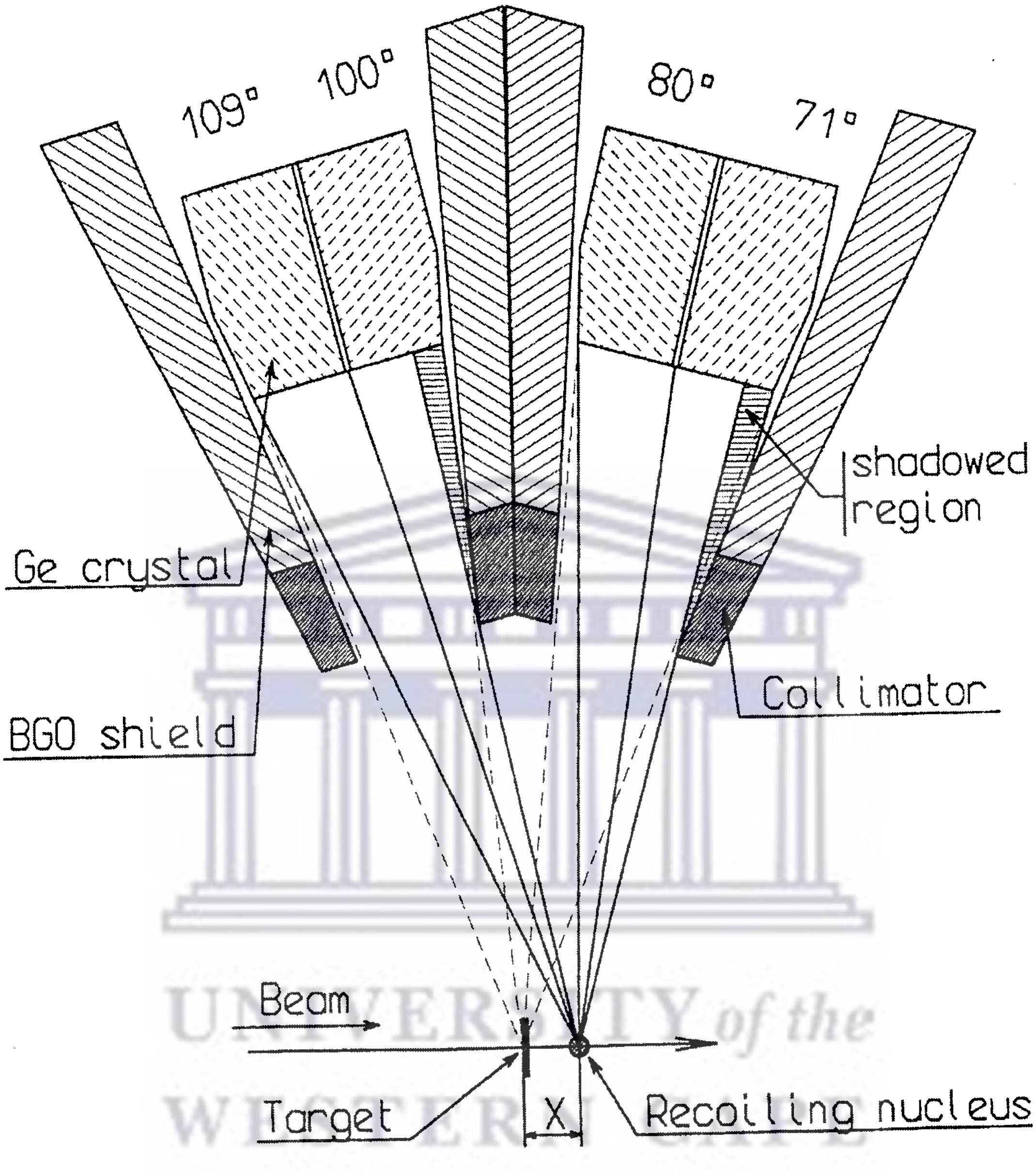

Figure 3.4: *Shadow effect of the collimators on the clovers of the Eurogam-II array. Shaded clover elements are at 71° and 100° and the unshaded at 80° and 109° [Gue01].*

Chapter 4

4 Data Analysis, Results and Summary

This chapter presents the experimental results on the linear polarization measurements and the lifetime measurements performed for the ^{194}Tl nuclei. For completeness some results of the $\gamma-\gamma$ coincidence and the DCO ratio measurements obtained by Ramashidzha et al [Ram06] are also included.

4.1 Linear Polarization Measurements in ^{194}Tl

The level scheme for ^{194}Tl extracted from the AFRODITE data is shown in fig. 4.1, considerably extending the previously known level scheme [Kre79] plotted in fig. 4.2. The level scheme and the spin assignments of the states were suggested by Ramashidzha et al [Ram06], and the parities of the levels were assigned in this work. Several collective structures were found and are labelled band 1, band 2, band 3 and band 4 [Ram06]. Transition energies, level spin and parity assignments, DCO ratios, linear polarization anisotropies, and multipolarities assigned to the γ-rays identified in ^{194}Tl are listed in Table 4.1. Fig. 4.3 and fig. 4.4 show two examples of polarization spectra used to measure the linear polarization anisotropies for the transitions of band 1 and band 2. These spectra are gated on the sum of 244+278+293 keV (band 1) and 154+304+360 keV (band 2) transitions respectively.

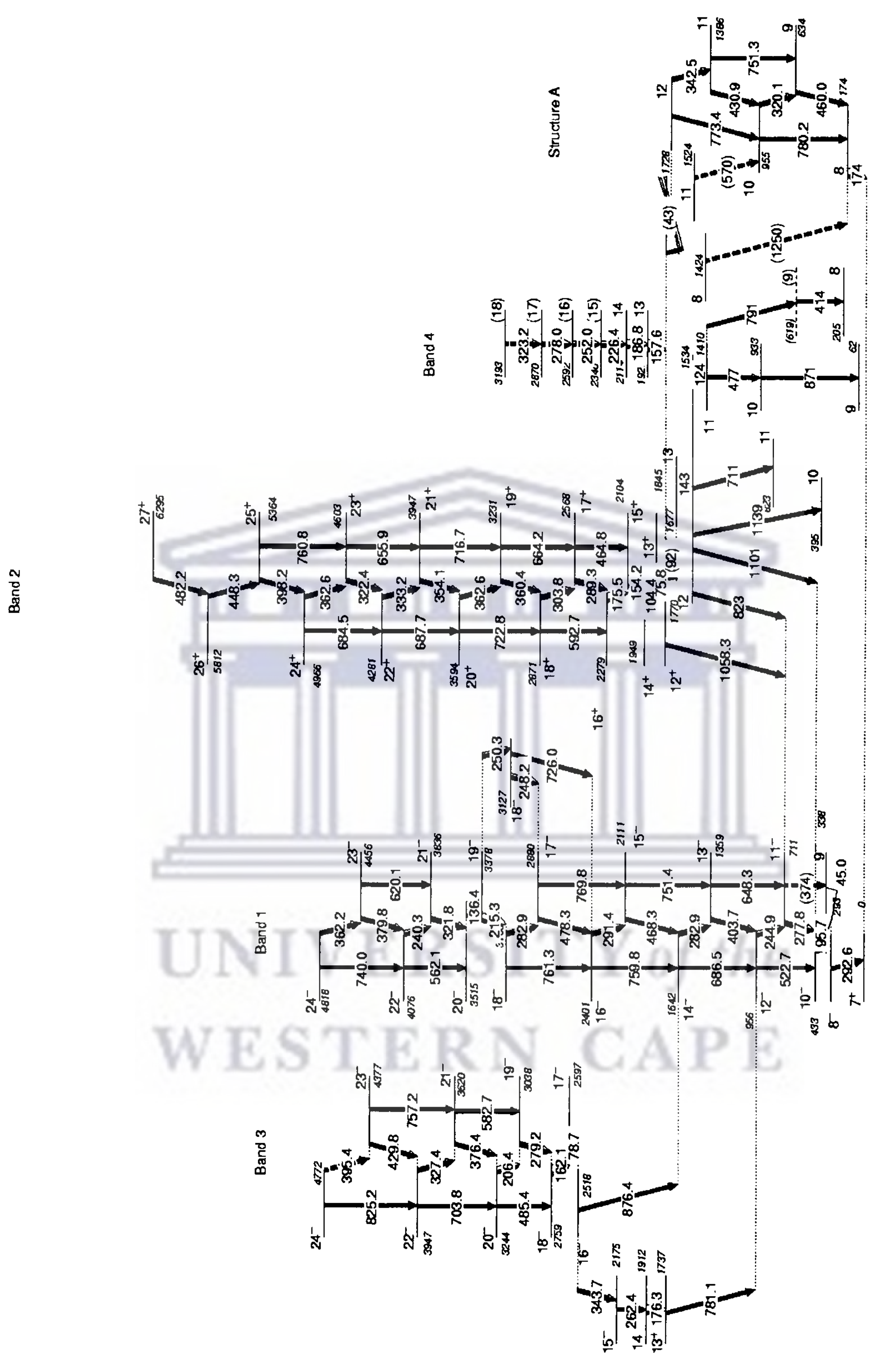

Figure 4.1: *The proposed level scheme of* ^{194}*Tl. The transition energies are given in keV. Tentative transitions are denoted with dashed lines and brackets [Ram06].*

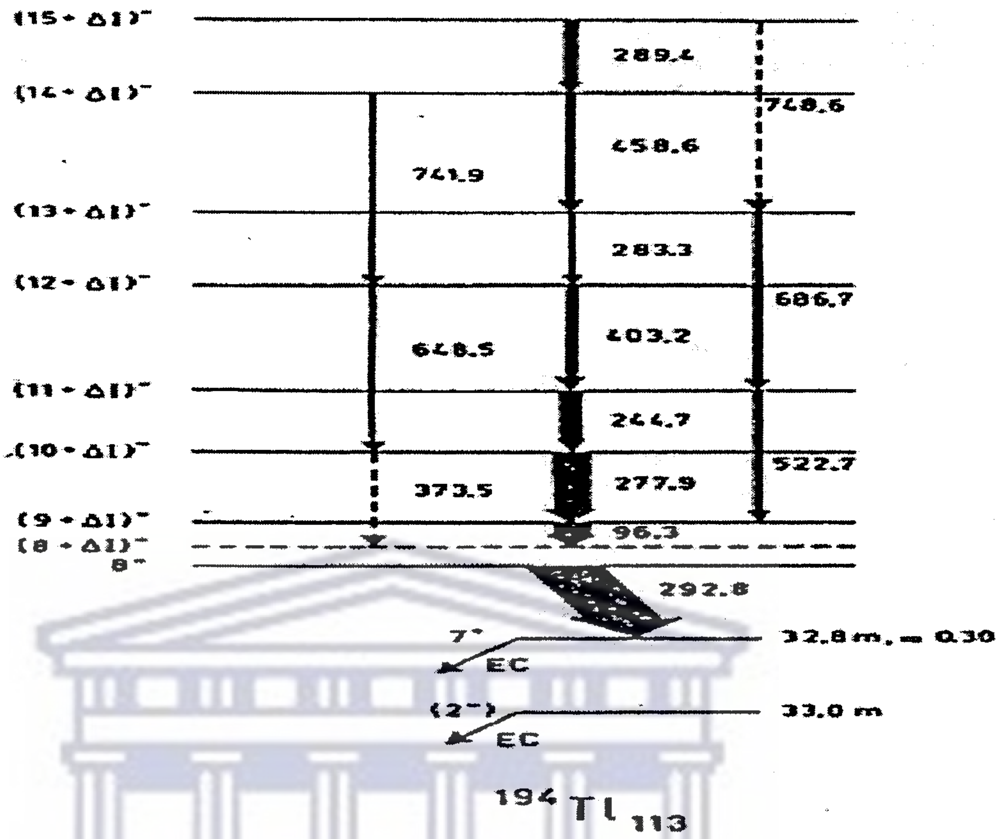

Figure 4.2: *The previously known level scheme of ^{194}Tl [Kre79].*

Table 4.1: *Gamma-ray energies, DCO ratios, linear polarization anisotropy, and the proposed spin and parity assignment for the transitions of ^{194}Tl.*

E_γ(keV) (*)	R_{DCO} (*)	A_p	Multipolarity	$J_i^\pi \rightarrow J_f^\pi$
42				$12^+ \rightarrow 12$
45.2	0.48(3)			$9^- \rightarrow 8^-$
75.8	0.52(3)			$13^+ \rightarrow 12^+$
78.7	0.49(7)			$17^- \rightarrow 18^-$
91.7	0.53(9)			$12^- \rightarrow (11)^-$
95.7	0.47(3)			$10^- \rightarrow 9^-$
104.4	0.50(7)			$14^+ \rightarrow 13^+$
124.5	0.50(6)			$(10) \rightarrow (9)$
136.4	0.54(6)			$20^- \rightarrow 19^-$
143.2	0.45(5)			$(11)^- \rightarrow (10)$
154.2	0.48(3)	-0.06(2)	M1	$15^+ \rightarrow 14^+$

157.6	0.52(8)			$14\rightarrow13^{+}$
162.1	0.48(2)			$18^{-}\rightarrow17^{-}$
174.3	0.46(10)			$8\rightarrow7^{+}$
175.5 Band2	0.47(2)	-0.02(1)	M1	$16^{+}\rightarrow15^{+}$
176.3 Band3	0.53(9)			$14^{+}\rightarrow13^{+}$
186.8	0.38(10)			$15\rightarrow14$
206.4	0.48(3)			$20^{-}\rightarrow19^{-}$
215.3	0.50(5)			$19^{-}\rightarrow18^{-}$
226.4	0.43(3)			$(16)\rightarrow15$
240.3	0.48(3)			$22^{-}\rightarrow21^{-}$
244.9	0.49(4)	-0.04(2)	M1	$12^{-}\rightarrow11^{-}$
248.2+250.3	0.44(4)			$18^{-}\rightarrow17^{-}, 19^{-}\rightarrow18^{-}$
262.4	0.47(6)			$15^{+}\rightarrow14^{+}$
277.8 Band1	0.51(3)	-0.05(1)	M1	$11^{-}\rightarrow10^{-}$
277.9 Band4	0.49(14)			$11^{-}\rightarrow10^{-}$
279.2	0.46(5)			$19^{-}\rightarrow18^{-}$
282.9+282.9	0.44(3)			$18^{-}\rightarrow17^{-}, 14^{-}\rightarrow13^{-}$
289.3	0.46(2)			$17^{+}\rightarrow16^{+}$
291.4	0.48(7)	-0.03(1)	M1	$16^{-}\rightarrow15^{-}$
293.4	0.61(7)	0.06(1)	E1	$8^{-}\rightarrow7^{+}$
303.8	0.46(2)	-0.03(1)	M1	$18^{+}\rightarrow17^{+}$
320.1	0.46(15)			$10\rightarrow9$
321.8 Band 1	0.54(12)	-0.03(2)	M1	$21^{-}\rightarrow20^{-}$
322.4 Band 2	0.51(18)	-0.07(2)	M1	$23^{+}\rightarrow22^{+}$
323.2	0.53(7)			$(17)\rightarrow(16)$
327.4	0.53(5)			$22^{-}\rightarrow21^{-}$
333.5	0.52(3)	-0.01(1)	M1	$22^{+}\rightarrow21^{+}$
342.5	0.45(4)	-0.07(2)	M1	$12\rightarrow11$
343.7	0.42(6)	-0.03(2)	M1	$16^{-}\rightarrow15^{-}$
354.1	0.40(3)	-0.04(1)	M1	$21^{+}\rightarrow22^{+}$
360.4	0.49(3)	-0.01(1)	M1	$19^{+}\rightarrow18^{+}$
361.8 Band1	0.49(2)			$24^{-}\rightarrow23^{-}$
362.6+362.6	0.50(3)			$20^{+}\rightarrow19^{+}, 24^{+}\rightarrow23^{+}$
376.4	0.48(3)			$21^{-}\rightarrow20^{-}$
379.8	0.46(4)			$23^{-}\rightarrow22^{-}$
395.4	0.48(8)	-0.03(2)	M1	$24^{-}\rightarrow23^{-}$
398.2	0.46(4)	-0.02(1)	M1	$25^{+}\rightarrow24^{+}$
403.4	0.41(2)	-0.02(1)	M1	$13^{-}\rightarrow12^{-}$
414.7	0.48(8)			$(7)\rightarrow(6)$
429.8	0.52(8)	- 0.03(2)	M1	$23^{-}\rightarrow22^{-}$
430.9	0.53(7)			$11\rightarrow10$
448.3	0.55(5)	-0.05(2)	M1	$26^{+}\rightarrow25^{+}$
459.8	0.51(5)	0.01(1)	E1	$9\rightarrow8$
464.8	0.82(3)			$17^{+}\rightarrow15^{+}$
468.4	0.45(4)	-0.05(1)	M1	$15^{-}\rightarrow14^{-}$

476.7	0.61(8)			$(9)\to(8)$
478.3	0.39(7)	-0.05(2)	M1	$17^{-}\to16^{-}$
482.2	0.36(6)			$27^{+}\to26^{+}$
485.4	0.83(10)	0.07(2)	E2	$20^{-}\to18^{-}$
522.7	0.78(16)	0.06(2)	E2	$12^{-}\to10^{-}$
562.8	0.72(8)	0.06(2)	E2	$22^{-}\to20^{-}$
569.6	0.81(31)			$\to10$
582.7	0.82(2)			$21^{-}\to19^{-}$
592.7	0.75(5)			$18^{+}\to16^{+}$
620.7	0.79(5)			$23^{-}\to21^{-}$
648.3	0.99(8)			$13^{-}\to11^{-}$
655.9	0.78(6)			$23^{+}\to21^{+}$
664.2	0.83(8)	0.06(2)	E2	$19^{+}\to17^{+}$
686.5	0.81(5)	0.07(1)	E2	$14^{-}\to12^{-}$
685.2+687.9	0.80(5)			$24^{+}\to22^{+},22^{+}\to20^{+}$
703.8	0.90(4)			$22^{-}\to20^{-}$
716.7	0.82(7)	0.07(2)	E2	$21^{+}\to19^{+}$
722.8	0.79(5)	0.01(2)	E2	$20^{+}\to18^{+}$
725.8	0.89(9)	0.06(2)	E2	$18^{-}\to16^{-}$
741.6	0.84(11)			$24^{-}\to22^{-}$
751.4 Band 1	0.82(11)	0.08(2)	E2	$15^{-}\to13^{-}$
751.3 Band 4	0.75(8)			$11\to9$
757.2	0.89(11)	0.06(2)	E2	$23^{-}\to21^{-}$
759.8+760.6	0.84(7)	0.06(2)	E2	$16^{-}\to14^{-}$
760.8 Band 2	0.75(5)	0.06(1)	E2	$25^{+}\to23^{+}$
769.7	0.70(4)	0.08(3)	E2	$17^{-}\to15^{-}$
773.4	0.78(5)	0.06(2)	E2	$12\to10$
780.2	0.65(6)	0.06(1)	E2	$10\to8$
781.1	0.42(9)	0.07(2)	E1	$13^{+}\to12^{-}$
790.6	0.80(7)			$11\to9$
822.6	0.76(9)			$10\to11^{-}$
825.2	0.84(11)	0.07(2)	E2	$24^{-}\to22^{-}$
871.2	0.65(9)			$(8)\to(7)$
876.4	0.88(7)	0.07(1)	E2	$16^{-}\to14^{-}$
1058.3	0.61(6)	0.02(2)	E1	$12^{+}\to11^{-}$
1100.8	0.69(9)			$(10)\to10^{-}$
1138.6	0.53(6)			$(10)\to(9)$
1162.6				

(*) Measured by Ramashidzha et al [Ram06]

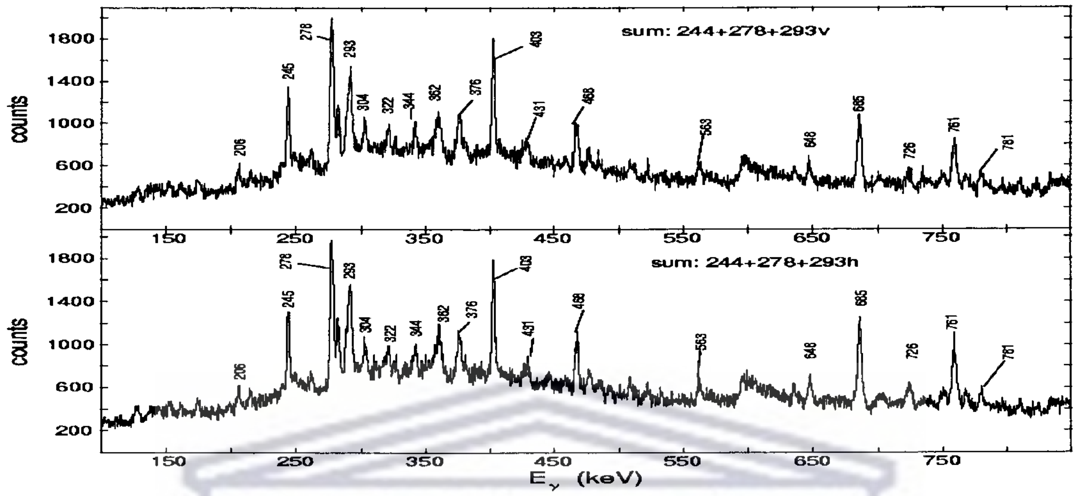

Figure 4.3: *Background – subtracted polarization spectra of vertically (top panel) and horizontally (bottom panel) scattered events, detected in the clovers at 90°, gated on the sum of 244, 277, and 293 keV transitions, and showing transitions from band 1.*

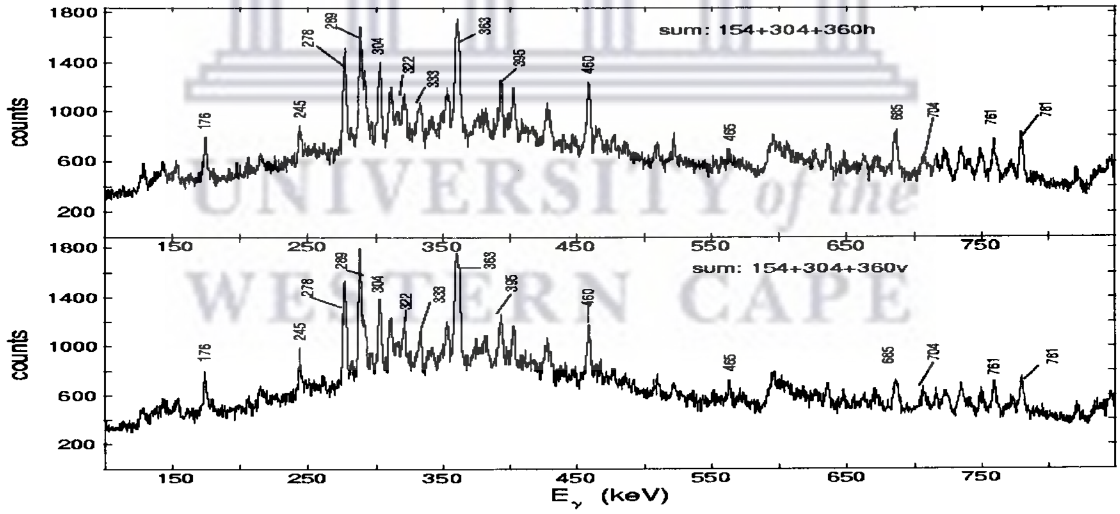

Figure 4.4: *Background – subtracted polarization spectra of horizontally (top panel) and vertically (bottom panel) scattered events, detected in the clovers at 90°, gated on the sum of 154, 303, and 360 keV transitions, and showing transitions from band 2.*

The measured linear polarization anisotropy as a function of the measured γ ray energy and R_{DCO} ratio for several transitions is presented in fig. 4.5 and fig. 4.6 respectively. In the present work, the DCO ratios and the linear polarization anisotropies were used to assign parities to the levels of ^{194}Tl.

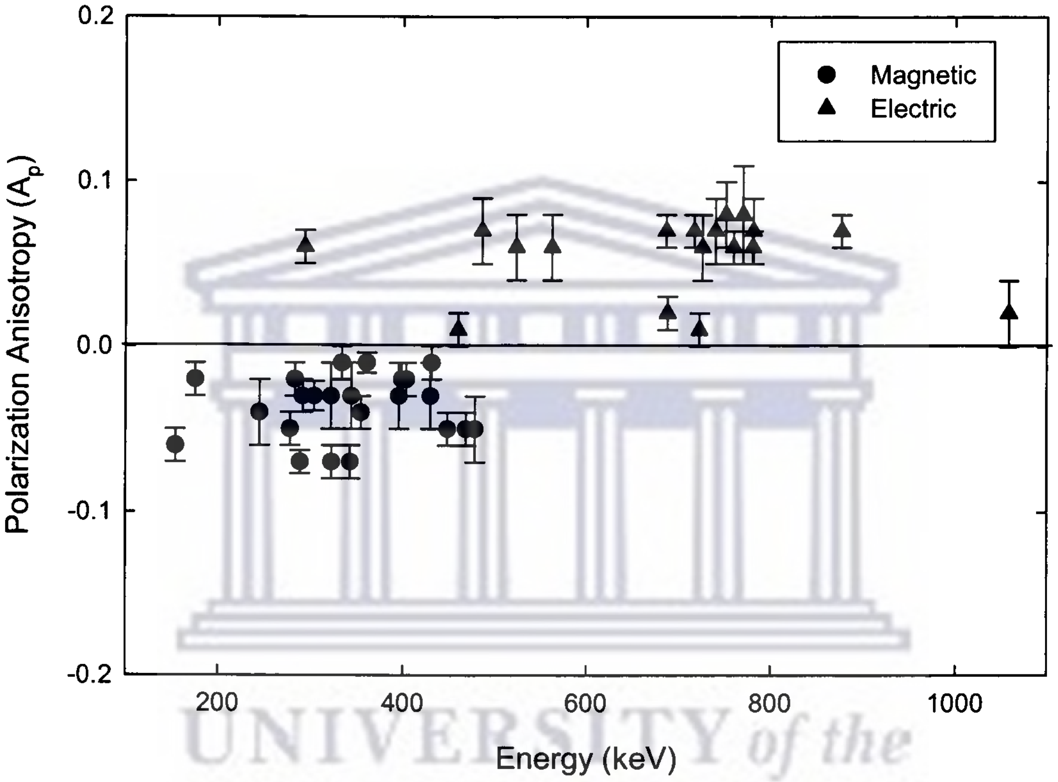

Figure 4.5: *The measured linear polarization anisotropy as a function of the γ – ray energy for several transitions in ^{194}Tl.*

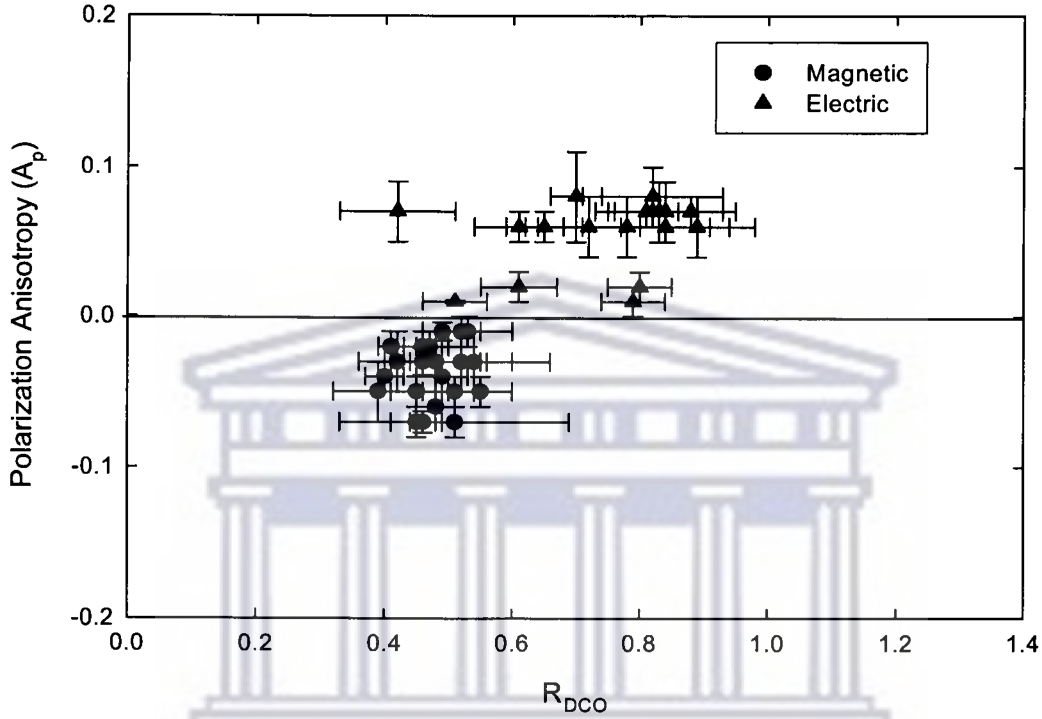

Figure 4.6. *The measured linear polarization anisotropy as a function of the measured* R_{DCO} *ratio for several transitions in* ^{194}*Tl. For the known dipole transitions* R_{DCO}~*0.5, for the known quadrupole transitions* R_{DCO}~*0.8 were found [Ram06].*

Band 1

Band 1 was extended up to a level with of $J^{\pi} = 24^{-}$ at an excitation energy of 4817.4 keV [Ram06]. The transitions of band 1 are shown in fig. 4.7 where a spectrum gated on the 293 keV γ ray is plotted. From the linear polarization measurements performed in this work electric character was deduced for the 293 keV decay out of the band - head of band1.Thus the previously assigned negative parity of the band is confirmed. The measured linear polarization anisotropies for direct and cross-over transitions in band 1 indicate magnetic and electric character respectively.

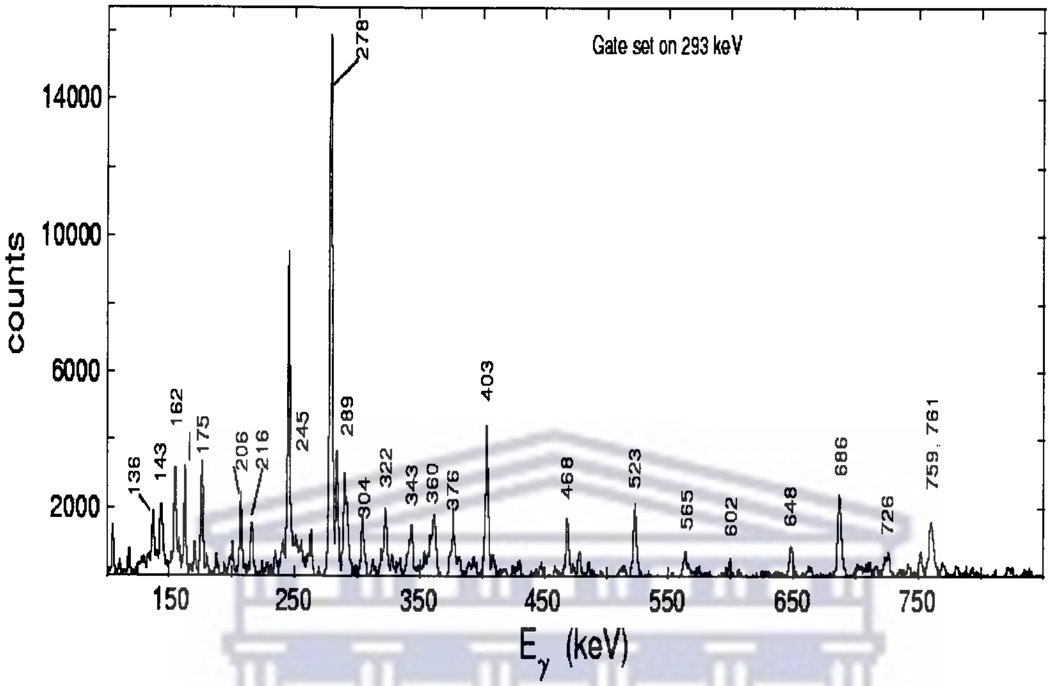

Figure 4.7: *The γ-ray coincidence spectrum with the gate set on the 293 keV transition. Data from both weekends.*

Band 2

A spectrum gated on the 1058 keV transition is plotted in fig. 4.8, showing the transitions of band 2. All parity assignments to band 2 were tentative in the previous work and based only on the systematics [Ram06]. In the present study, the parity assignments to these states come from measured linear polarization anisotropies.

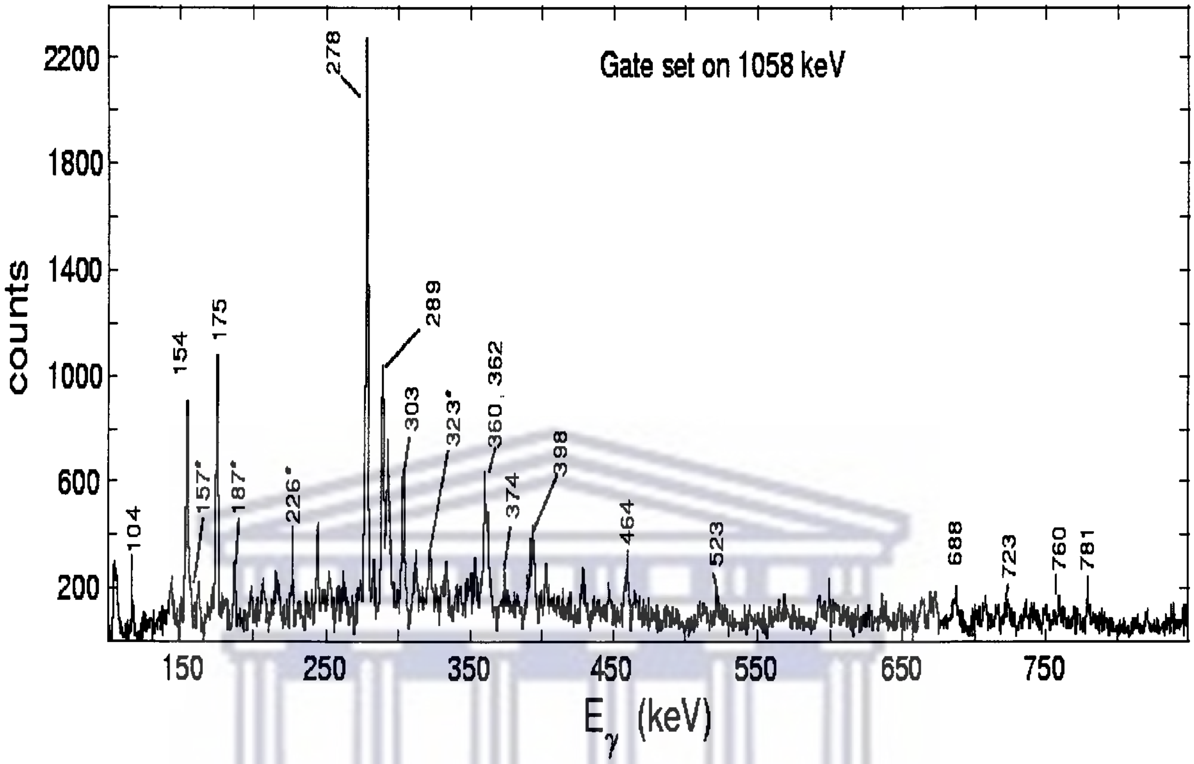

Figure 4.8: *The γ -rays coincidence spectrum gated on the 1058 keV transition. The transitions from band 4 are marked with stars. Data from both weekends.*

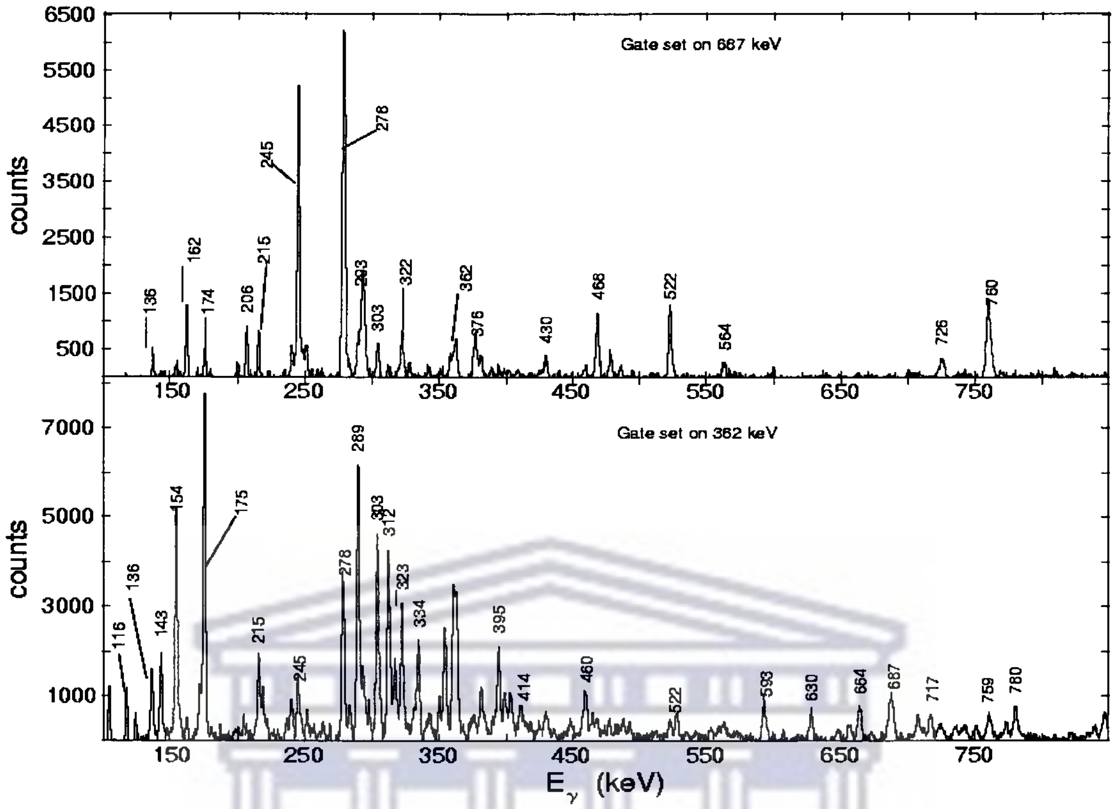

Figure 4.9: *Spectra gated on the 687 keV (top panel) and 362 keV(bottom panel) transitions. Data from both weekends.*

The 1058 keV γ ray was found to be consistent with stretched E1 character by measuring its DCO ratio [Ram06] and linear polarization anisotropy in this work, which leads to the establishment of a $J^\pi = 12^+$ assignment for the state at excitation energy of 1770 keV. Consequently positive parities are assigned for the states of band 2. The measured linear polarization anisotropies for the direct and cross over transitions of this band indicate magnetic and electric nature respectively. Linear polarization measurements for low-energy transitions are very difficult because of low statistics, due to small Compton scattering probabilities.

Band 3

This band decays to the $J^{\pi} = 12^{-}$ and $J^{\pi} = 14^{-}$ levels of band 1. The band 3 transitions are shown in fig. 4.10 where a spectrum gated on the 162 keV $\gamma -$ ray, is plotted. Negative parity was previously associated with band 3 [Ram06], because of the suggested quadrupole character of the 876 keV γ ray and based on the consideration that if this transition was of M2 nature a long lifetime would be expected. In this work positive linear polarization anisotropy was measured for the 876 keV γ ray, thus confirming its E2 nature and the negative parity of band 3. The linear polarization anisotropy of the transitions of band 3 are consistent with M1 and E2 characters for the direct and crossover transitions respectively. The band extends up to the 24^{-} level.

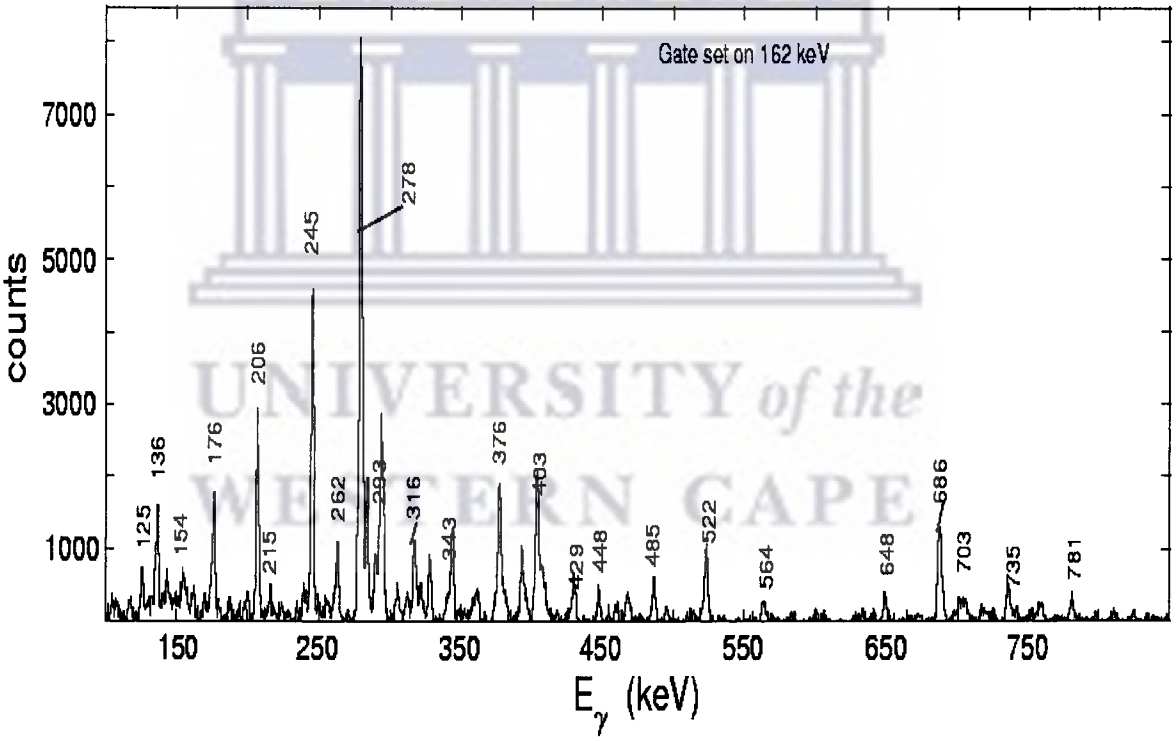

Figure 4.10: *The γ-rays coincidence spectrum gated on the 162 keV transition. Data from both weekends.*

Band 4 and structure A.

Band 4 is based on the $J^{\pi} = 12^{+}$ level and it consists of very few transitions. The transitions for band 4 are shown in fig. 4.8, and marked by stars. The linear polarization anisotropies for these transitions could not be determined since the transitions are very weak. Thus no parity is assigned to this band.

4.2.3 Lifetime Measurements for ^{194}Tl

RSAM as described in section 3.2.9 was used to search for nanosecond isomeric states in ^{194}Tl. RSAM was performed by analysing spectra associated with either the clover elements at 84° (shaded elements) or with the clover elements at 96° (unshaded elements) relative to the beam axis. The experimental anisotropy A_{RSAM} for delayed transitions was calculated from the expression

$$A_{RSAM} = \frac{\alpha N_U - N_S}{\alpha N_U + N_S} \tag{4.1}$$

with relative efficiency $\alpha = 0.64$ for gated spectrum, where N_u denotes the number of γ-rays detected in the un-shaded clover elements, and N_s the number detected in the shaded elements. The sum and difference spectra (corresponding to the denominator and the numerator of the above expression), gated on the 278 keV transition are shown in fig. 4.11. Only one isomeric state is observed associated with the 293 keV ($8^{-} \rightarrow 7^{+}$, band 1) delayed γ ray as seen in fig. 4.11.

In addition, fig. 4.12 shows the time spectra obtained from the clovers for the 278, 293 and 303 keV ($18^{+} \rightarrow 17^{+}$, band 2) γ rays. From these spectra, it can clearly be seen that the 293 keV γ ray transition is delayed since its time peak has a tail towards longer lifetimes when compared to the time peaks of the other two transitions. These spectra are shown in logarithmic scale in fig. 4.13

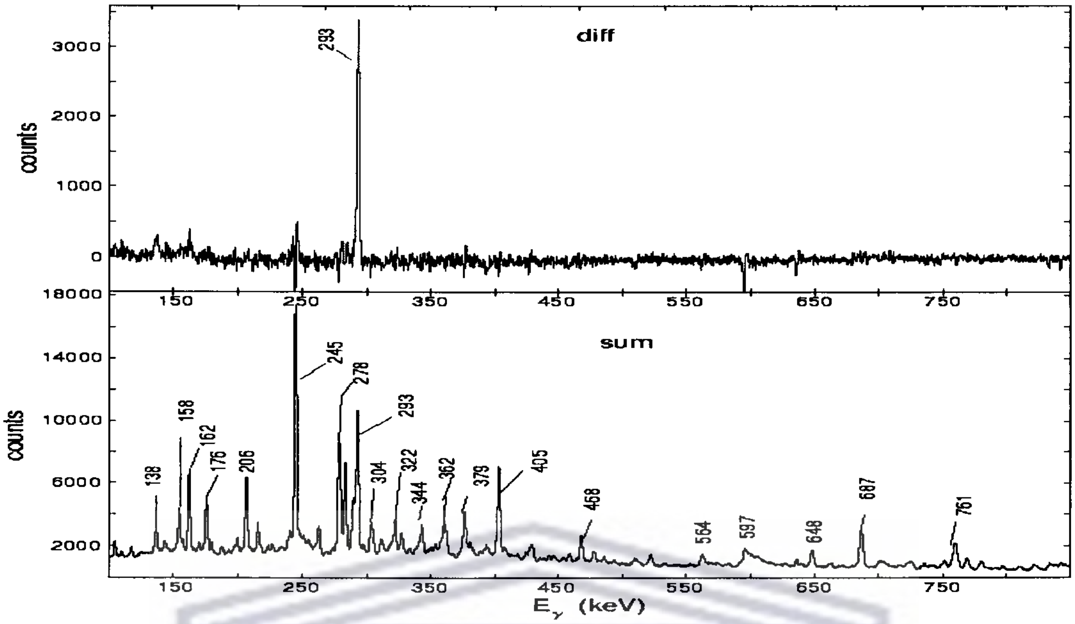

Figure 4.11: *Difference (top panel) and sum (bottom panel) spectra gated on the 278 keV γ-ray.*

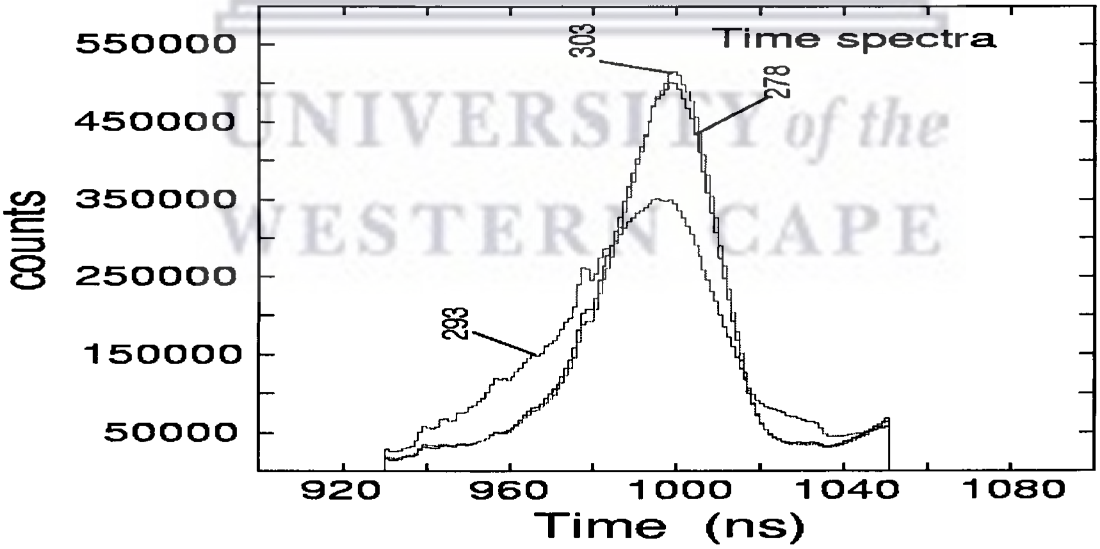

Figure 4.12: *Time spectra for the 278 (band 1), 293 (band 1) and 303 (band 2) keV transitions.*

The measured RSAM anisotropy for the 293 keV transition using spectra gated on the 278 keV and 876 keV transitions are: $A_{RSAM}(293, g278) = 32 \pm 2$ % and $A_{RSAM}(293, g876) = 34 \pm 2$ %. All transitions of band 1 are in coincidence with the 278 keV transition. It should be noted that there is a prompt 291 keV γ ray in band 1. Therefore the measured anisotropy of the 293 keV might be underestimated in this gated spectrum. The 876 keV gate was therefore chosen because it is in coincidence with the 293 keV γ ray and is in anticoincidence with the 291 keV transition. In order to extract the half-life of this isomer using the obtained value of the anisotropy, the calibration curve for the AFRODITE array was used. Figure 4.14 shows the calibration curve for the AFRODITE array [Gue03]. The measured anisotropy value of 34 % corresponds to $vt_{1/2} = 16.5$ mm. Using the value of the recoil velocity $v/c = 0.80 \pm 0.04\%$, $t_{1/2} = 6.9 \pm 1$ ns was deduced.

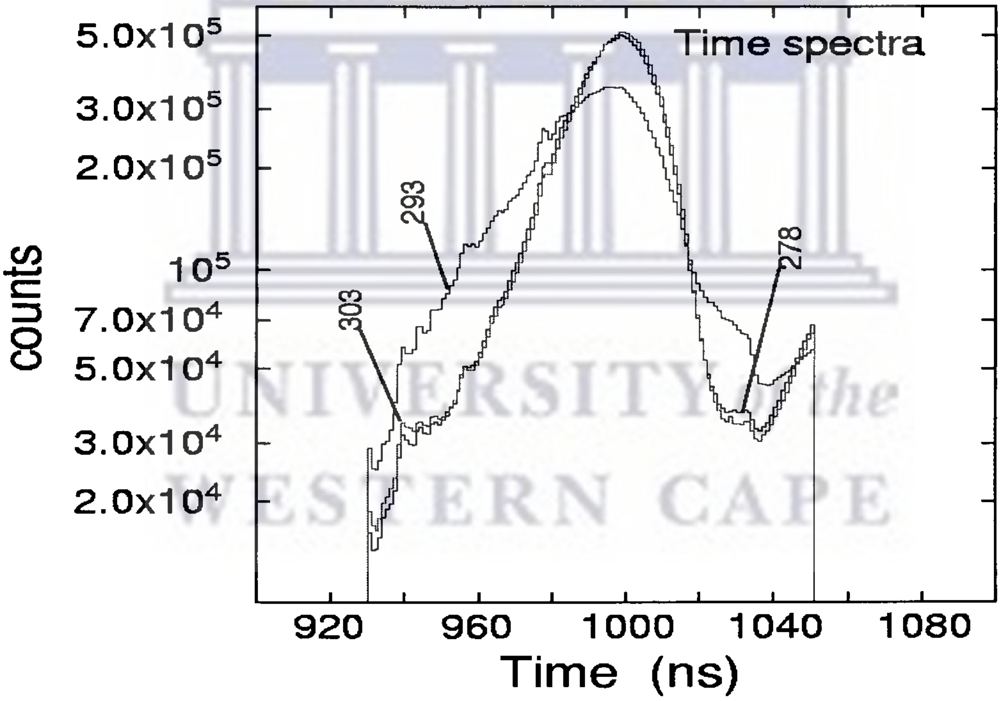

Figure 4:13: *Time spectra for the 278, 293 and 303 keV transitions, shown in log scale.*

In the previous study [Kre79], the half life of the 293 keV γ ray was estimated from intensity balance considerations and found to lie in the 15 – 40 ns interval. Such a figure was found to coincide well with what is expected from the $B(E1)$ values of ^{198,196}Tl (i.e., $t_{1/2} \approx$ 30 nsec) and also fits into the statistics of hindered $E1$ transitions. In the present study, a more accurate value of $t_{1/2}$= 6.9±1.0 ns was derived using the RSAM method. A measurement of this half-life using time – difference spectra is also planned.

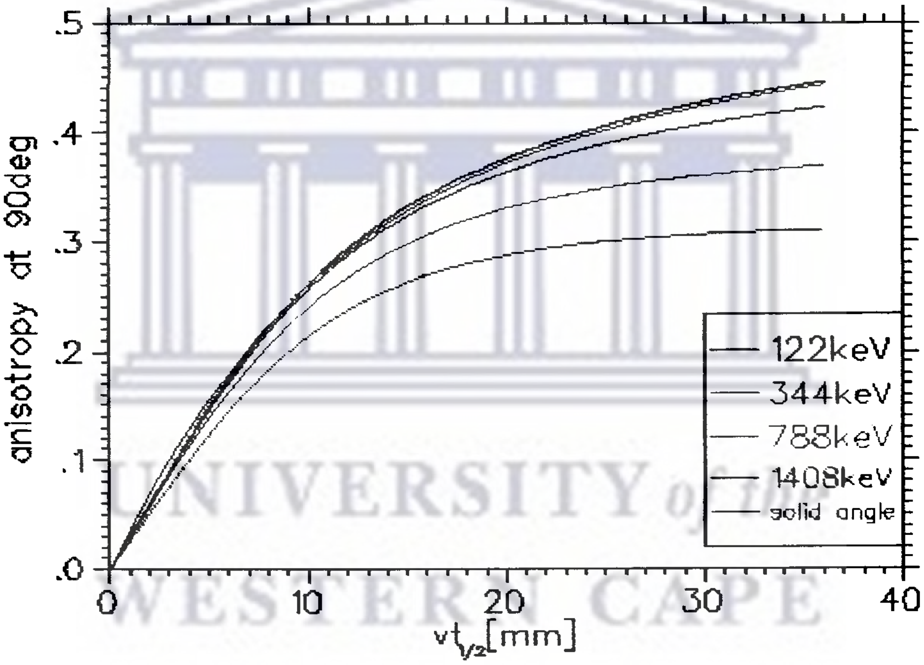

Figure 4.14: *The AFRODITE array RSAM calibration curve. From [Gue03]*

4.2 Summary

The work presented in this thesis is based on the analysis of the AFRODITE γ-spectroscopy data for ^{194}Tl. These data were obtained using the ^{181}Ta(^{18}O,5n)^{194}Tl reaction at a beam energy of 91 and 93 MeV during two week-ends beam time. In this work gain matching, calibration, gain drift corrections, Doppler-shift corrections were performed for one week-end data. Then the whole data set was sorted into gamma-gamma, DCO, polarization matrices and time spectra. Then linear polarization measurements and Recoil Shadow Anisotropy (RSAM) lifetime measurements were performed using the whole data set. The aim of this study was to measure the linear polarization coefficients and to search for nanosecond isomers using the RSAM [Gue01] technique in ^{194}Tl nuclei. The polarization measurements have supported the parity assignments suggested for the existing level scheme [Ram06]. In addition, parities were measured for the levels of band 2. The magnetic and the electric character of many of the observed γ-ray transitions was determined and multipolarities of mostly stretched M1, E1 and E2 were assigned. One isomeric state was observed in ^{194}Tl using RSAM. This further lends support to observations made in a previous study [Kre79] in which the 293 keV γ ray showed a marked decrease in its intensity relative to other lines known to belong to ^{194}Tl. In the present work the half-life of the observed isomeric state was extracted using the RSAM AFRODITE array calibration curve to be $t_{1/2} = 6.9 \pm 1.0$ ns. This value is more accurate than the previous estimation of 15-40ns [Kre79]. Further measurements of this lifetime are planned using time – difference spectra.

References

[Bea96] C.W. Beausang and J. Simpson, J. Phys. G. Nucl. Part. Phys. 22, 527 (1996).

[Bre01] J. T. Breitweg, PhD thesis, Department of physics, University of Wisconsin-Madison, 2001.

[But73] P. A. Butler, P. E. Carr, L. L. Gardeken, A. N. James, P. J. Nolan, J. F. Sharpey-Schafer, P. J. Twin and D. A. Viggars, Nucl. Instr. and Meth. 108, 497 (1973).

[Dir90] M. W. Drigert, M. Piiparinen, R. V. F. Janssens, R. Holzmann, I. Ahmad, J. Borggreen, R. R. Chasman, P. J. Daly, B. K. Dichter, H. Emling, U. Garg, Z. W. Grabowski, T. L. Khoo, W. C. Ma, M. Quader, D. C. Radford and W. Trzaska, Nucl. Phys. A 515, 466 (1990).

[Duc99] G. Duchene et al., Nucl. Instr. and Meth. in Phys. Res. A 432, (1999) 90 110.

[Dup02] J. Duprat, These IPNO-T-95.2002.

[Eml86] H. Emling, F. Azgui, M. Däther, S. Doebereiner, H. Grein, C. Michel and H. J. Wollersheim, Nucl. Instr. and Meth. in Phys. Res. A249, 320 (1986).

[Fag59] L. W. Fagg and S. S. Hanna, Rev. Mod. Phys. 31, 711 (1959).

[Fra86] D. A. Fraser, The Physics of Semiconductor Devices, Fourth Edition, Oxford University Press (1986).

[Gav80] A. Gavron, Phys. Rev. C 23, 920 (1992).

[Gav93] A. Gavron, Computational Nuclear Physics 2, Nuclear Reactions, Springer- Verlag New York, Inc, 108 (1993).

[Gil95] G. Gilmore and J. D. Hemingway, Practical Gamma-Ray Spectrometry, Wiley (1995).

[Gon76] Y. Gono, R. M. Lieder, M. Müller-Veggian, A. Neskakis, C. Mayer-Böricke, Phys. Rev. Lett. 37 (1976) 1123.

[Gro67] J. R. Grover, Phys. Rev. 157, 832 (1967).

[Gue00] E. Gueorguieva et al., Physica Scripta T88, 135 (2000).

[Gue01] E. Gueorguieva, M. Kaci, C. Schück, A. Minkova, Ch. Vieu, J. J. Correia and J. S. Dionisio, Nucl. Instr. and Meth. in Phys. Res. A 474, 132 (2001).

[Gue03] E. Gueorguieva et al, iThemba LABS Annual Report 2003, iThemba LABS PAC Report, May 2003.

[Jos97] P. K. Joshi et al., Nucl. Instr. and Meth. in Phys. Res. A 399, 51 (1997).

[Kno89] G. F. Knoll, Radiation Detection and Measurement, Second Edition, Wiley (1989).

[Kra73] K. S. Krane, R. M. Steffen and R. M. Wheeler, Nuclear Data Tables, 11, 351 (1973).

[Kre77] A. J. Kreiner, M. Fenzl, S. Lunardi and M. A. J. Mariscotti, Nucl. Phys. A 282 (1977) 243.

[Kre78] A. J. Kreiner, M. Fenzl, and W. Kutschera, Nucl. Phys. A 308 (1978) 147.

[Kre79] A. J. Kreiner, M. Fenzl, U. Heim and W. Kutschera, Phys. Rev. C20 (1979)

2205.

[Kre80] A. J. Kreiner et al., Phys. Rev. C21 (1980) 933.

[Lie75] R. M. Lieder, H. Beuscher, W. F. Davidson, A. Neskakis, C. Mayer Böricke, Nucl. Phys. A 248 (1975) 317.

[Lie76] R. M. Lieder, in Proc. Int. Symp. On collectivity of medium and heavy nuclei, Tokyo, (1976), ed. Y. Shida, p459.

[Lie84] R. M. Lieder, H. Jäger, A. Neskakis, T. Venkova and C. Michel, Nucl. Instr. and Meth. in Phys. Res. A 220, 363 (1984).

[Lie95] R. M. Lieder, Experimental Techniques in Nuclear Physics (Walter de Gruyter, Berlin, 1995).

[Lil01] J. S. Lilley "Nuclear Physics Principles and Applications", John Wiley & Sons, 2001.

[Lit70] A. E. Litherland, G. T. Ewan and S. T. Lam, Canadian Journal of Phys. 48 2320 (1970).

[Mey74] J. Meyer-ter-Vehn, F. S. Stephens, R. M. Diamond, Phys. Rev. Lett. 32 (1974) 1383.

[New70] J. O. Newton, S. D. Cirilov, F. S. Stephens, R. M. Diamond, Nucl. Phys. A 148 (1970) 593.

[New74] J. O. Newton, F. S. Stephens, R. M. Diamond, Nucl. Phys. A 236 (1974) 225.

[New98] R. T. Newman et al., Balkan Phys. Lett. Special Issue, 182 (1998).

[Nil95] S. G. Nilsson and Ragnarsson "Shapes and Shells in the Nuclear Structure" Cambridge University Press. (1995).

[Nol94] P. J. Nolan et al., Annual Rev. Nucl. Part. Sci A 45 516-607 (1994).

[Pro74] D. Proetel, D. Benson Jr., A. Gizon, J. Gizon, M. R. Maier, R. M. Diamond

F. S. Stephens, Nucl. Phys. A 226 (1974) 237.

[Rad95] D. C. Radford, Nucl. Instr. Methods Phys. Res. A 361, 297 (1995).

[Ram06] T. M. Ramashidzha, M Sc thesis, Department of Physics, University of the Western Cape, unpublished, 2006.

[Rou01] D. G. Roux, Ph.D. Thesis, University of Cape Town, unpublished, (2001).

[Sch81] J. P. Schiffer, Italian Physical Society, *Proceedings of the International School of Physics, Enrico Fermi*, Course LXXVΠ, Villa Monastero, 205 (1979).

[Sch94] B. Schlitt, U. Maier, H. Friedrichs, S. Albers, I. Bauske, P. von Brentano, R. D. Herzberg, U. Kneissl, J. Margraf, H. H. Pitz, C. Wesselborg and A. Zilges, Nucl. Instr. and Meth. in Phys. Res. A337, 416 (1994).

[Sch98] G. J. Schlitt, A. O. Macchiavelli, S. J. Asztalos, R. M. Clark, M. A. Deleplanque, R. M. Diamond, P. Fallon, R. Kruecken, I. Y. Lee, R. W. MacLeod, F. S. Stephens and K. Vetter, Nucl. Instr. and Meth. A417, 95 (1998).

[Sim83] J. Simpson and P. A. Butler, Nucl. Instr. and Meth. 204, 463 (1983).

[Szy83] Z. Szymanski in "Fast Nuclear Rotations" Clarendon Press. Oxford (1983).

[Tjø74] P. O. Tjøm, M. R. Maier, D. Benson, Jr., F. S. Stephens, R. M. Diamond, Nucl. Phys. A231 (1974) 397.

[Tok75] H. Toki, A. Faessler, Nucl. Phys. A 253 (1975) 231.

[Wil82] J. Wilczynski *et. al.*, Nucl. Phys. A 373 (1982) 109.